FISEVIER

Contents lists available at ScienceDirect

Computers and Mathematics with Applications

journal homepage: www.elsevier.com/locate/camwa



Forward and inverse modeling of fault transmissibility in subsurface flows $^{\stackrel{\wedge}{}}$



Jeonghun J. Lee ^{a,*,1}, Tan Bui-Thanh ^{b,d,2}, Umberto Villa ^{d,1}, Omar Ghattas ^{c,d,1}

- ^a Department of Mathematics, Baylor University, Waco, TX, USA
- ^b Department of Aerospace Engineering and Engineering Mechanics, UT Austin, Austin, TX, USA
- c Walker Department of Mechanical Engineering, UT Austin, Austin, TX, USA
- ^d The Oden Institute for Computational Engineering and Sciences, UT Austin, Austin, TX, USA

ARTICLE INFO

ABSTRACT

Keywords: Subsurface flow Fault transmissibility Inverse problem Characterizing physical properties of faults, such as their transmissibility, is crucial for performing predictive numerical simulation of subsurface flows, such as those encountered in petroleum engineering and remediation of subsurface contamination. This paper provides a complete investigation of the inverse problem for fault transmissibility in subsurface flow models, under appropriate assumptions on fault structure. In particular, the following aspects are considered: 1) fault modeling and well-posedness of the forward problem; 2) finite element (FEM) discretizations of the forward problem and their rigorous *a priori* convergence analysis; 3) Well-posedness of the Bayesian inverse problem, FEM discretization of the infinite dimensional Bayesian inverse formulation, and its rigorous *a priori* analysis. Moreover, computation of the *maximum a posteriori* (MAP) point via fast inexact Newton-conjugate gradient optimization and a Laplace approximation of the Bayesian posterior are also presented. Numerical results illustrate the use of the proposed fault model in forward and inverse problems for subsurface flows in two dimensional domains with multiple faults.

1. Introduction

Accurate modeling and numerical simulation of subsurface flows are important for such applications as reservoir engineering, contaminant transport, groundwater management, and carbon sequestration. In subsurface flow models, the fault (or fracture) structure has a great influence on the fluid flow. Therefore, modeling fault structures with appropriate physical parameters is important for accurate simulations of subsurface flows when fault structures exist in the subsurface domain (see, e.g., [1–4] and more references in a recent review article [5]).

Faults in oil reservoirs can be complex geometric structures with relatively thin volumes compared to the entire domain of a reservoir model. Therefore, high resolution modeling of faults as volumetric objects requires very fine meshes to describe the full geometric complexity of faults. Such an approach, though providing high fidelity simulations,

comes at the expense of extremely high computational costs. Moreover, detailed information for high resolution models of faults is usually not available in practical applications. Existing approaches typically model a fault as a manifold of codimension one in the entire domain. This is meaningful as the thickness of faults is negligibly small compared to the length scale of the entire reservoir model [6–8]. In this paper, we also adopt this approach for modeling fault structures.

Some previous studies on subsurface flow models with faults consider a geometric multiscale framework in which specifically designed interface conditions are used to couple the flow equations in the whole domain with those in the fault domains [6,7]. In this paper, we assume that the permeabilities of faults are much lower than the surrounding media, and thus fluid does not flow along fault structures [9]. As a consequence, we obtain a reduced single-phase flow model that does not require the velocity and the pressure fields on faults as independent

^{*} This work was partially supported by ExxonMobil through its membership in The University of Texas at Austin Energy Institute.

^{*} Corresponding author.

E-mail addresses: jeonghun_lee@baylor.edu (J.J. Lee), tanbui@oden.utexas.edu (T. Bui-Thanh), uvilla@oden.utexas.edu (U. Villa), omar@oden.utexas.edu

¹ J.L., U.V., and O.G. were partially supported by the Department of Energy award DE-SC0019303.

² T.B.T is partially funded by the National Science Foundation awards NSF-OAC-2212442, NSF-2108320, NSF-1808576 and NSF-CAREER-1845799; by the Department of Energy award DE-SC0018147 and DE-26083989; and by 2020 ConTex award; and by 2021 UT-Portugal CoLab award.

unknowns. Moreover, the physical parameters associated with the permeability of faults are reduced to the fault transmissibility fields (see Section 2 and [9]).

In this paper we discuss fault modeling and numerical methods together with their analyses for both forward simulation and inversion of the fault transmissibility from well data for the aforementioned single-phase subsurface flow model. For discretization of the forward model, one can use many different numerical methods such as the mixed method [6,9], the multipoint flux approximation [9], the finite volume method [7], and the mimetic finite difference method [10]. In this paper we use the mixed finite element method, since it is well-supported by FEniCS [11,12] and hIPPYlib [13,14], the two open source software packages for finite element methods and Bayesian inversion problems, respectively, that we use for numerical results.

The remainder of the paper is organized as follows. In Section 2 we present function space notation, derive the single-phase forward partial differential equation (PDE) model of subsurface flow in domain with faults, and show its Babuška–Brezzi stability. In Section 3 we discretize the model with mixed finite elements and prove *a priori* error estimates. In Section 4 we first present an infinite Bayesian inversion framework and show its well-posedness. This is followed by FEM discretizations of the prior and the likelihood and their error analyses. We then combine prior and likelihood discretizations to construct an FEM discretization of the infinite dimensional Bayesian posterior measure and provide its convergence analysis. Computation of the MAP point via a fast inexact Newton-conjugate gradient optimization method, followed by Laplace approximation of the Bayesian posterior, are also presented. Numerical results illustrating our theoretical findings are presented in Section 5. Section 6 concludes the paper with future research directions.

2. Preliminaries

2.1. Notation

Let Ω be a bounded domain in \mathbb{R}^n with n=2 or 3. For a nonnegative integer m, $H^m(\Omega)$, $H^m(\Omega;\mathbb{R}^n)$ denote the standard \mathbb{R} and \mathbb{R}^n -valued Sobolev spaces based on L^2 norm, and $\|\cdot\|_m$ with $m\geq 0$ the scalar- or vector-valued H^m -norms. Boldface letters are reserved for vector-valued functions.

For functions $f, g \in L^2(\Omega)$ and $f, g \in L^2(\Omega; \mathbb{R}^n)$ let

$$(f,g) := \int_{\Omega} fg \, dx, \qquad (f,g) := \int_{\Omega} f \cdot g \, dx.$$

Similarly, for an (n-1)-dimensional submanifold $D \subset \Omega$ and functions $f,g \in L^2(D), \, f,g \in L^2(D;\mathbb{R}^n)$ we define

$$\langle f, g \rangle_D := \int\limits_D f \cdot g \, ds, \qquad \langle f, g \rangle_D = \int\limits_D f \cdot g \, ds.$$

2.2. Modeling fault transmissibility

In this section we derive the fault transmissibility model under the assumption of an infinitesimal fault thickness. Let us consider the model domain illustrated in Fig. 1 comprising two subdomains Ω_+ (the right subdomain in Fig. 1) and Ω_- (the left subdomain in Fig. 1) divided by a fault domain Γ_f (the middle subdomain in Fig. 1) with thickness d_f . For simplicity we assume that the two interfaces $\Gamma_+ := \partial \Omega_+ \cap \partial \Gamma_f$, $\Gamma_- := \partial \Omega_- \cap \partial \Gamma_f$ are parallel to each other. The constant permeability parameters on the subdomains are κ_+ , κ_- , κ_f , respectively, and p_+ , p_- are the pressure values on the interfaces Γ_+ , Γ_- . We denote by n the unit normal vector field on Γ_+ from Γ_f to Ω_+ . We assume that fluid flows follow the Darcy law, i.e., the velocity of the fluid is $-\kappa \nabla p$ for a pressure field p. Here we assume that the pressure field p is continuous, so if we denote the pressure field in the fault of thickness d_f by p_f , then $p_- = p_f|_{\Gamma_-}$ and $p_+ = p_f|_{\Gamma_+}$. We also assume that Γ_f is thin and $\kappa_f \ll \kappa_+, \kappa_-$,

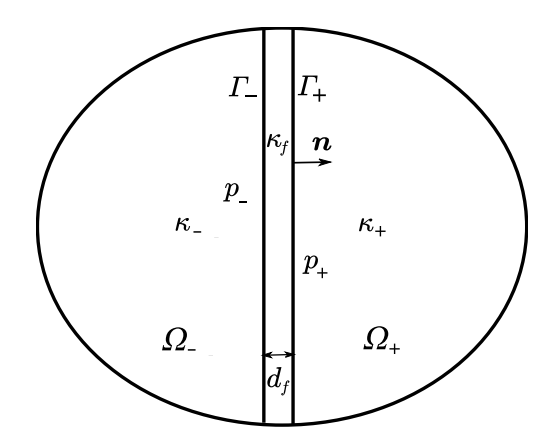


Fig. 1. Modeling of fault.

so the fault has no absorption, drainage of fluids, and tangential fluid flows. By this assumption and flux conservation

$$-(\kappa_{+}\nabla p)\cdot \boldsymbol{n}|_{\Gamma_{+}} = -(\kappa_{f}\nabla p_{f})\cdot \boldsymbol{n}|_{\Gamma_{+}}, \quad -(\kappa_{-}\nabla p)\cdot \boldsymbol{n}|_{\Gamma_{-}} = -(\kappa_{f}\nabla p_{f})\cdot \boldsymbol{n}|_{\Gamma_{-}}.$$

By the fundamental theorem of calculus along the direction orthogonal to Γ_+ , we have

$$-\kappa_f(p_+ - p_-) = -\int\limits_{-d_f/2}^{d_f/2} (\kappa_f \nabla p_f) \cdot \boldsymbol{n} \, dl.$$

In our modeling, d_f is small, so we may assume that κ_f is nearly a constant on the fault. The approximation of the above integral with the trapezoidal rule and the flux continuity give

$$-\kappa_f(p_+ - p_-) \approx -\frac{d_f}{2}((\kappa_+ \nabla p) \cdot \boldsymbol{n}|_{\Gamma_+} + (\kappa_- \nabla p) \cdot \boldsymbol{n}|_{\Gamma_-}).$$

The difference between p_+ and p_- is thus not negligible. In addition, since we assume that there is no tangential flow along the fault, we have

$$(\kappa_+ \nabla p) \cdot \boldsymbol{n}|_{\Gamma_-} = (\kappa_- \nabla p) \cdot \boldsymbol{n}|_{\Gamma_-}$$

which results in the following constitutive equation for the fault

$$[[p]] := p_+ - p_- = t_f(\kappa_+ \cdot \nabla p) \cdot \mathbf{n}|_{\Gamma_+} = t_f(\kappa_- \cdot \nabla p) \cdot \mathbf{n}|_{\Gamma_-}, \qquad t_f = \frac{d_f}{\kappa_f}. \tag{1}$$

Since d_f is much smaller than the characteristic length scale of our subsurface model, Γ_f is considered as a zero thickness fault in our partial differential equation model in Section 2.3.

2.3. Partial differential equation model (forward problem)

A fault Γ is a union of disjoint (n-1)-dimensional Lipschitz submanifolds in Ω and we denote $\Omega \setminus \Gamma$ by $\mathring{\Omega}$. We assume that there exist open subdomains $\Omega_+, \Omega_- \subset \mathring{\Omega}$ with Lipschitz boundaries such that $\overline{\Omega} = \overline{\Omega_+} \cup \overline{\Omega_-}$, $\Gamma \subset \partial \Omega_+ \cap \partial \Omega_-$, and only one side of Γ is in contact with Ω_+ or Ω_- . Let n_+ and n_- be the two unit normal vector fields on Γ with opposite directions $(n_+ = -n_-)$ such that n_+ correspond to the unit outward normal vector fields from Ω_+ . Suppose that Γ_D and Γ_N are (n-1)-dimensional open submanifolds on $\partial \Omega$ such that $\overline{\Gamma_D} \cup \overline{\Gamma_N} = \partial \Omega$ and $\Gamma_D \cap \Gamma_N = \emptyset$. Here we use the convention that (\cdot, \cdot) is the integration on Ω and $\langle \cdot, \cdot \rangle_{\Gamma}$ is the integration on Γ .

We also assume that

(A1) for any $q \in L^2(\Omega)$ there exists $\mathbf{w} \in H^1(\Omega; \mathbb{R}^n)$ such that $\mathbf{w}|_{\Gamma} = 0$, div $\mathbf{w} = q$, and $\|\mathbf{w}\|_1 \le C\|q\|_0$, with a constant C > 0 depending only on Ω and Γ .

The assumption (A1) holds, for instance, if both of $\partial\Omega_+ \cap \partial\Omega$ and $\partial\Omega_- \cap \partial\Omega$ have positive (n-1)-dimensional Lebesgue measures. A proof can be found in [15, Corollary 2.4].

Let $\gamma_+: H^1(\Omega_+) \to H^{1/2}(\Gamma)$ and $\gamma_-: H^1(\Omega_-) \to H^{1/2}(\Gamma)$ be the trace operators. For a function $p \in H^1(\mathring{\Omega})$, we define p_+ on the fault Γ as

$$p_{-}(x) = \gamma_{-}p$$
, $p_{+}(x) = \gamma_{+}p$, $\forall x \in \Gamma$.

Suppose that $t_f > 0$ is a fault transmissibility function on Γ and u is a vector-valued function on Ω such that $u \cdot n_+ = -u \cdot n_-$ is single-valued on Γ .

Assume that κ is a symmetric positive definite permeability tensor on Ω . The pressure and flux boundary conditions are given as g_D on Γ_D and g_N on Γ_N . Recalling (1), for pressure p and flux $u=-\kappa\nabla p$ in $\mathring{\Omega}$, a mixed formulation of the Darcy equation in domain Ω with fault Γ reads:

$$\kappa^{-1} \mathbf{u} + \nabla p = 0 \quad \text{in } \mathring{\Omega}, \qquad \text{div } \mathbf{u} = f \quad \text{in } \mathring{\Omega},$$
(2a)

$$\boldsymbol{u} \cdot \boldsymbol{n} = g_N \quad \text{on } \Gamma_N, \qquad p = g_D \quad \text{on } \Gamma_D,$$
 (2b)

$$\mathbf{u} \cdot \mathbf{n} - t_f^{-1}[[p]] = 0 \quad \text{on } \Gamma.$$
 (2c)

Hereafter, we assume that $\Gamma_D=\partial\Omega$ and $g_D=0$ for simplicity of exposition. Let $Q=L^2(\Omega)$, and $H(\operatorname{div},\Omega)$ be the space of \mathbb{R}^n -valued L^2 functions on Ω such that its distributional divergence is in $L^2(\Omega)$. We define V as

$$V = \{ v \in H(\text{div}, \Omega) : v \cdot n|_{\Gamma} \in L^2(\Gamma) \}$$

and the norm on V is defined by

$$\|\mathbf{v}\|_{\mathbf{V}} = \left(\|\mathbf{v}\|_{0}^{2} + \|\operatorname{div}\mathbf{v}\|_{0}^{2} + \|\mathbf{v}\cdot\mathbf{n}\|_{0,\Gamma}^{2}\right)^{\frac{1}{2}}$$

where $\|q\|_{0,\Gamma}:=\langle q,q\rangle_{\Gamma}^{1/2}$. Here we derive a variational formulation with the interior Robin-type boundary condition (2c) on Γ with an additional regularity assumptions on the exact solutions \mathbf{u} and p. More specifically, we assume that the exact solutions \mathbf{u} and p satisfy $p\in H^1(\mathring{\Omega})$ and $\mathbf{u}\in V$ with additional regularity satisfying (2c) almost everywhere on Γ . We remark that this approach is inspired by [16] on mixed finite element methods for Robin boundary condition problems.

From integration by parts of the first equation in (2a), we have

$$\int\limits_{\Omega} \kappa^{-1} \boldsymbol{u} \cdot \boldsymbol{v} \, dx - \int\limits_{\Omega} p \operatorname{div} \boldsymbol{v} \, dx + \left\langle p_{+}, \boldsymbol{v} \cdot \boldsymbol{n}_{+} \right\rangle_{\Gamma} + \left\langle p_{-}, \boldsymbol{v} \cdot \boldsymbol{n}_{-} \right\rangle_{\Gamma} = 0 \qquad \forall \boldsymbol{v} \in \boldsymbol{V},$$

which, after invoking $\boldsymbol{v} \cdot \boldsymbol{n}_+ = -\boldsymbol{v} \cdot \boldsymbol{n}_-$, $\langle p_+, \boldsymbol{v} \cdot \boldsymbol{n}_+ \rangle_{\Gamma} + \langle p_-, \boldsymbol{v} \cdot \boldsymbol{n}_- \rangle_{\Gamma} = \langle [\![p]\!], \boldsymbol{v} \cdot \boldsymbol{n}_+ \rangle_{\Gamma}$, and $\boldsymbol{u} \cdot \boldsymbol{n}_+ - t_f^{-1}[\![p]\!] = 0$, becomes

$$\int_{\Omega} \kappa^{-1} \boldsymbol{u} \cdot \boldsymbol{v} \, dx - \int_{\Omega} p \operatorname{div} \boldsymbol{v} \, dx + \left\langle t_f \boldsymbol{u} \cdot \boldsymbol{n}_+, \boldsymbol{v} \cdot \boldsymbol{n}_+ \right\rangle_{\Gamma} = 0 \qquad \forall \boldsymbol{v} \in \boldsymbol{V}.$$
 (3)

In the following, we use $\langle t_f \boldsymbol{u} \cdot \boldsymbol{n}, \boldsymbol{v} \cdot \boldsymbol{n} \rangle_{\Gamma}$ to denote $\langle t_f \boldsymbol{u} \cdot \boldsymbol{n}_+, \boldsymbol{v} \cdot \boldsymbol{n}_+ \rangle_{\Gamma}$ since the bilinear form $\langle t_f \boldsymbol{u} \cdot \boldsymbol{n}, \boldsymbol{v} \cdot \boldsymbol{n} \rangle_{\Gamma}$ is the same for $\boldsymbol{n} = \boldsymbol{n}_+$ and $\boldsymbol{n} = \boldsymbol{n}_-$. In the final variational formulation the exact solution $(\boldsymbol{u}, \boldsymbol{p})$ satisfies

$$\begin{cases} \left(\kappa^{-1}\boldsymbol{u},\boldsymbol{v}\right) - (p,\operatorname{div}\boldsymbol{v}) + \left\langle t_f\boldsymbol{u}\cdot\boldsymbol{n},\boldsymbol{v}\cdot\boldsymbol{n}\right\rangle_{\Gamma} &= 0 & \forall \boldsymbol{v}\in\boldsymbol{V}, \\ (\operatorname{div}\boldsymbol{u},q) &= (f,q) & \forall q\in\boldsymbol{Q}. \end{cases}$$
 (4)

The system (4) can be viewed as a saddle point problem

$$\begin{cases}
 a(u,v) + b(v,p) &= F(v), \\
 b(u,q) &= G(q)
\end{cases}$$
(5)

with the two bilinear forms and two linear forms

$$\begin{split} a\left(\boldsymbol{u},\boldsymbol{v}\right) &= \left(\kappa^{-1}\boldsymbol{u},\boldsymbol{v}\right) + \left\langle t_{f}\boldsymbol{u}\cdot\boldsymbol{n},\boldsymbol{v}\cdot\boldsymbol{n}\right\rangle_{\Gamma}, \qquad b(\boldsymbol{v},q) = -\left(\operatorname{div}\boldsymbol{v},q\right), \\ F(\boldsymbol{v}) &= 0, \qquad G(q) = -(f,q). \end{split}$$

Theorem 1. Suppose that $\|t_f\|_{L^{\infty}(\Gamma)}, \|t_f^{-1}\|_{L^{\infty}(\Gamma)} < +\infty$ and F and G are bounded linear functionals on V and $L^2(\Omega)$ in (5). Then, (5) has a unique solution $(u,p) \in V \times L^2(\Omega)$.

Proof. By the definition of $||v||_V$ it is easy to check

$$|a(v,v')| \le ||a|| ||v||_V ||v'||_V, \qquad |b(v,q)| \le ||v||_V ||q||_0$$

with

$$||a|| := \max\{||\kappa^{-1}||_{L^{\infty}(\Omega)}, ||t_f||_{L^{\infty}(\Gamma)}\}.$$
 (6)

By (A1) we can obtain the inf-sup condition for the Babuška–Brezzi stability theory (cf. [17])

$$\inf_{q \in \mathcal{Q}} \sup_{v \in V} \frac{b(v, q)}{\|v\|_V \|q\|_0} \ge \beta > 0 \tag{7}$$

where β depends on Ω . Since we assume $\|t_f^{-1}\|_{L^\infty(\Gamma)} < +\infty$ the coercivity

$$\inf_{v \in Z} \frac{a(v, v)}{\|v\|_{V}^{2}} \ge \alpha > 0, \qquad Z := \{v' \in V : \operatorname{div} v' = 0\}$$
 (8)

with $\alpha = \min\{\|\kappa\|_{L^{\infty}(\Omega)}^{-1}, \|t_f^{-1}\|_{L^{\infty}(\Gamma)}^{-1}\}$, is obtained by

$$\begin{split} a(\boldsymbol{v}, \boldsymbol{v}) &= \left(\kappa^{-1} \boldsymbol{v}, \boldsymbol{v}\right) + \left\langle t_f \boldsymbol{v} \cdot \boldsymbol{n}, \boldsymbol{v} \cdot \boldsymbol{n} \right\rangle_{\Gamma} \\ &\geq \min\{\|\kappa\|_{L^{\infty}(\Omega)}^{-1}, \|t_f^{-1}\|_{L^{\infty}(\Gamma)}^{-1}\} \left(\|\boldsymbol{v}\|_0^2 + \|\boldsymbol{v} \cdot \boldsymbol{n}\|_{0,\Gamma}^2\right) \\ &\geq \min\{\|\kappa\|_{L^{\infty}(\Omega)}^{-1}, \|t_f^{-1}\|_{L^{\infty}(\Gamma)}^{-1}\} \|\boldsymbol{v}\|_V^2 \end{split}$$

for $v \in Z$. Then, the well-posedness of (4) follows from the Babuška–Brezzi theory [17]. \square

For an analysis of inverse problem presented in Section 4, we claim that the solution of (5) depends continuously on t_f under additional assumptions.

Theorem 2. Suppose that $m, \tilde{m} \in L^{\infty}(\Gamma)$. and (u, p) and (\tilde{u}, \tilde{p}) in $V \times Q$ are the solutions of (5) for $t_f = e^m$ and $t_f = e^{\tilde{m}}$, respectively. Then there exist constants C_1 and C_2 depending on $\|\kappa^{-1}\|_{L^{\infty}(\Omega)}$, $\|m\|_{L^{\infty}(\Gamma)}$, and $\|\tilde{m}\|_{L^{\infty}(\Gamma)}$ such that

$$\|\mathbf{u} - \tilde{\mathbf{u}}\|_{V} + \|p - \tilde{p}\|_{0} \le C_{1} \|t_{f} - \tilde{t}_{f}\|_{L^{\infty}(\Gamma)} \le C_{2} \|m - \tilde{m}\|_{L^{\infty}(\Gamma)}.$$

Proof. For $t_f = e^m$ and $\tilde{t}_f = e^{\tilde{m}}$ the coercivity constants of $a(\cdot, \cdot)$ are

$$\alpha = \min\{\|\kappa\|_{L^{\infty}(\Omega)}^{-1}, e^{-\|m\|_{L^{\infty}(\Gamma)}}\}, \quad \tilde{\alpha} = \min\{\|\kappa\|_{L^{\infty}(\Omega)}^{-1}, e^{-\|\tilde{m}\|_{L^{\infty}(\Gamma)}}\}.$$

By [17, Theorem 4.2.3], the solution (u, p) of (5) satisfies

$$\|\mathbf{u}\|_{V} \le \frac{1}{\alpha} \|F\|_{V'} + \frac{2\|a\|^{1/2}}{\alpha^{1/2}\beta} \|G\|_{0},$$
 (9)

$$||p||_{0} \le \frac{2||a||^{1/2}}{\sigma^{1/2} \beta} ||F||_{V'} + \frac{||a||}{\beta^{2}} ||G||_{0}$$
(10)

with α , β , ||a|| in (8), (7), (6) where

$$\|F\|_{V'} := \sup_{\boldsymbol{v} \in V} \frac{F(\boldsymbol{v})}{\|\boldsymbol{v}\|_{V}}, \qquad \|G\|_{0} := \sup_{q \in L^{2}(\Omega)} \frac{G(q)}{\|q\|_{0}}.$$

From (5) it is easy to see that

$$\left(\kappa^{-1}(\boldsymbol{u}-\tilde{\boldsymbol{u}}),\boldsymbol{v}\right) + \left\langle t_f\left(\boldsymbol{u}-\tilde{\boldsymbol{u}}\right)\cdot\boldsymbol{n},\boldsymbol{v}\cdot\boldsymbol{n}\right\rangle_{\Gamma} + b(p-\tilde{p},\boldsymbol{v}) + b(\boldsymbol{u}-\tilde{\boldsymbol{u}},q)$$

$$= -\left\langle (t_f - \tilde{t}_f)\tilde{\boldsymbol{u}} \cdot \boldsymbol{n}, \boldsymbol{v} \cdot \boldsymbol{n} \right\rangle_{\Gamma}.$$

By (9), (10),

$$\begin{aligned} \|\boldsymbol{u} - \tilde{\boldsymbol{u}}\|_{V} &\leq \frac{1}{\alpha} \sup_{\boldsymbol{v} \in V} \frac{-\left\langle (t_{f} - \tilde{t}_{f})\tilde{\boldsymbol{u}} \cdot \boldsymbol{n}, \boldsymbol{v} \cdot \boldsymbol{n} \right\rangle_{\Gamma}}{\|\boldsymbol{v}\|_{V}} \\ &\leq \frac{1}{\alpha} C(m, \tilde{m}) \|m - \tilde{m}\|_{L^{\infty}(\Gamma)} \|\tilde{\boldsymbol{u}} \cdot \boldsymbol{n}\|_{L^{2}(\Gamma)}, \end{aligned}$$

and similarly,

$$\|p-\tilde{p}\|_0 \leq \frac{2\|a\|^{1/2}}{\alpha^{1/2}\beta}C(m,\tilde{m})\|m-\tilde{m}\|_{L^\infty(\Gamma)}\|\tilde{\boldsymbol{u}}\cdot\boldsymbol{n}\|_{L^2(\Gamma)}.$$

Finally, $\|\tilde{\boldsymbol{u}} \cdot \boldsymbol{n}\|_{L^2(\Gamma)}$ is bounded by the formulas (9) with F = 0, G = f where $\|\boldsymbol{a}\|$ and α are replaced by

$$\|\tilde{a}\| := \max\{\|\kappa^{-1}\|_{L^{\infty}(\Omega)}, \|\tilde{t}_f\|_{L^{\infty}(\Gamma)}\},$$

and \tilde{a} , which leads to the conclusion. \square

3. Discretization with mixed methods and the a priori error analysis

In this section we discuss the finite element discretization and the a priori error analysis of (4). Throughout this section we assume that Ω is a bounded domain with a polygonal/polyhedral boundary.

Let \mathcal{T}_h be a triangulation of Ω with n-dimensional simplices without hanging nodes with discretization parameter h>0 which is the maximum diameter of n-dimensional simplices in \mathcal{T}_h . \mathcal{E}_h is the corresponding set of (n-1)-dimensional simplices generated by \mathcal{T}_h . We always assume that a subset of \mathcal{E}_h , denoted by \mathcal{E}_h^{Γ} , forms a triangulation of the fault Γ , and \mathcal{T}_h is shape-regular with an upper-bound of shape regularity that is uniform in h (cf. [18]).

For an integer $k \ge 0$ and a set $D \subset \mathbb{R}^n$, $\mathcal{P}_k(D)$ is the space of polynomials defined on D of degree at most k. Similarly, $\mathcal{P}_k(D;\mathbb{R}^n)$ is the space of \mathbb{R}^n -valued polynomials of degree at most k. For given $k \ge 1$ let us define

$$\boldsymbol{V}_h^{RTN}(T) = \mathcal{P}_{k-1}(T; \mathbb{R}^n) + \begin{pmatrix} x_1 \\ \vdots \\ x_n \end{pmatrix} \mathcal{P}_{k-1}(T),$$

$$V_h^{BDM}(T) = \mathcal{P}_k(T; \mathbb{R}^n), \qquad T \in \mathcal{T}_h.$$

Suppose that $V_h \subset V$ is the Raviart–Thomas–Nedelec (RTN) or Brezzi–Douglas–Marini (BDM) element (see, e.g., [17] for details) defined by

$$\boldsymbol{V}_h = \{\boldsymbol{v} \in \boldsymbol{V} \ : \ \boldsymbol{v}|_T \in \boldsymbol{V}_h^{RTN}(T), \quad \forall T \in \mathcal{T}_h\},$$

or
$$V_h = \{ v \in V : v|_T \in V_h^{BDM}(T), \forall T \in \mathcal{T}_h \}.$$

The finite element space Q_h is defined by

$$Q_h = \{q \in Q \ : \ q|_T \in \mathcal{P}_{k-1}(T) \quad \forall T \in \mathcal{T}_h\}.$$

Then ${\rm div}\, V_h = Q_h$ and it is well-known that the pair (V_h,Q_h) satisfies (7) with a discrete inf-sup constant $\bar{\beta}$ independent of h [17, p. 406].

The discretization of (4) is to seek $(\boldsymbol{u}_h, p_h) \in \boldsymbol{V}_h \times Q_h$ such that

$$\begin{cases} (\kappa^{-1}\boldsymbol{u}_{h},\boldsymbol{v}) - (p_{h},\operatorname{div}\boldsymbol{v}) + \langle t_{f}\boldsymbol{u}_{h}\cdot\boldsymbol{n},\boldsymbol{v}\cdot\boldsymbol{n}\rangle_{\Gamma} &= 0 & \forall \boldsymbol{v}\in\boldsymbol{V}_{h}, \\ (\operatorname{div}\boldsymbol{u}_{h},q) &= (f,q) & \forall q\in\boldsymbol{Q}_{h}. \end{cases}$$
(11)

Since (7) and (8) hold with (V_h,Q_h) , well-posedness and the stability of this system follow from the standard Babuška-Brezzi theory.

3.1. The a priori error analysis

For error analysis we consider the difference of (4) and (11) which reads

$$(\kappa^{-1}(\boldsymbol{u} - \boldsymbol{u}_h), \boldsymbol{v}) - (p - p_h, \operatorname{div} \boldsymbol{v})$$
(12a)

$$+ \langle t_f(\mathbf{u} - \mathbf{u}_h) \cdot \mathbf{n}, \mathbf{v} \cdot \mathbf{n} \rangle_{\Gamma} = 0 \qquad \forall \mathbf{v} \in \mathbf{V}_h,$$

$$(\operatorname{div}(\mathbf{u} - \mathbf{u}_h), q) = 0 \qquad \forall q \in Q_h. \tag{12b}$$

Let Π_h be the canonical interpolation operator into V_h by the standard degrees of freedom and P_h be the L^2 projection into Q_h . Then it is known (cf. [17]) that

$$P_h \operatorname{div} \mathbf{v} = \operatorname{div} \Pi_h \mathbf{v} \tag{13}$$

holds for $v \in V \cap L^r(\Omega; \mathbb{R}^n)$, r > 2.

Theorem 3. Suppose that (u, p) and (u_h, p_h) are the solutions of (4) and (11). Assuming that u and p are sufficiently regular to make the norms below well-defined, then

$$\left\| \kappa^{-1/2} (\mathbf{u} - \mathbf{u}_h) \right\|_0 + \left\| t_f^{1/2} (\mathbf{u} - \mathbf{u}_h) \cdot \mathbf{n} \right\|_{0,\Gamma}$$
 (14)

$$\leq \begin{cases} Ch^{k-1/2} \left\| \boldsymbol{u} \right\|_{k} & \text{ if } \boldsymbol{V}_{h} \text{ is RTN element} \\ Ch^{k+1/2} \left\| \boldsymbol{u} \right\|_{k+1} & \text{ if } \boldsymbol{V}_{h} \text{ is BDM element} \end{cases}$$

$$\|p - p_h\|_0 \le \begin{cases} Ch^{k-1/2} \left(\|u\|_k + \|p\|_k \right) & \text{if } V_h \text{ is RTN element} \\ Ch^k (\|u\|_{k+1/2} + \|p\|_k) & \text{if } V_h \text{ is BDM element} \end{cases}.$$
 (15)

Proof. We decompose the errors as the following

$$\mathbf{u} - \mathbf{u}_h = (\mathbf{u} - \Pi_h \mathbf{u}) + \underbrace{(\Pi_h \mathbf{u} - \mathbf{u}_h)}_{e} = : (\mathbf{u} - \Pi_h \mathbf{u}) + e_{\mathbf{u}}$$

$$p - p_h = (p - P_h p) + \underbrace{(P_h p - p_h)}_{e_p} = : (p - P_h p) + e_p.$$

From (12b) $P_h \operatorname{div} \mathbf{u} = \operatorname{div} \mathbf{u}_h$ holds, therefore $\operatorname{div} e_{\mathbf{u}} = 0$ by the definition of $e_{\mathbf{u}}$. Taking $\mathbf{v} = e_{\mathbf{u}}$ in (12a), we have

$$(\kappa^{-1}e_{\mathbf{u}}, e_{\mathbf{u}}) + \langle t_f e_{\mathbf{u}} \cdot \mathbf{n}, e_{\mathbf{u}} \cdot \mathbf{n} \rangle_{\Gamma}$$

$$= -(\kappa^{-1}(\mathbf{u} - \Pi_h \mathbf{u}), e_{\mathbf{u}}) - \langle t_f (\mathbf{u} - \Pi_h \mathbf{u}) \cdot \mathbf{n}, e_{\mathbf{u}} \cdot \mathbf{n} \rangle_{\Gamma}. \quad (16)$$

Applying the Cauchy–Schwarz inequality to (16) we obtain

$$\begin{aligned} \left\| \kappa^{-1/2} e_{\boldsymbol{u}} \right\|_{0} + \left\| t_{f}^{1/2} e_{\boldsymbol{u}} \cdot \boldsymbol{n} \right\|_{0,\Gamma} \\ &\leq 2 \left\| \kappa^{-1/2} (\boldsymbol{u} - \Pi_{h} \boldsymbol{u}) \right\|_{0} + 2 \left\| t_{f}^{1/2} (\boldsymbol{u} - \Pi_{h} \boldsymbol{u}) \cdot \boldsymbol{n} \right\|_{0,\Gamma}. \end{aligned}$$

The interpolation Π_h gives an optimal order of approximation in $L^2(\Omega)$ [17] but we lose 1/2 order in the approximation of $\left\|t_f^{1/2}e_u\cdot n\right\|_{0,\Gamma}$ because of the scaling factor in trace inequalities in the theory of finite element methods (cf. [19, Lemma 1.49]).

Assuming that u is sufficiently regular, we obtain error estimates

$$\left\|\kappa^{-1/2}e_{\pmb{u}}\right\|_0 + \left\|t_f^{1/2}e_{\pmb{u}}\cdot \pmb{n}\right\|_{0,\Gamma} \leq \begin{cases} Ch^{k-1/2}\,\|\pmb{u}\|_k & \text{if } \pmb{V}_h \text{ is RTN element} \\ Ch^{k+1/2}\,\|\pmb{u}\|_{k+1} & \text{if } \pmb{V}_h \text{ is BDM element} \end{cases}$$

where C>0 depends on $\left\|\kappa^{-1}\right\|_{L^{\infty}}$ and $\left\|t_f\right\|_{L^{\infty}}$. Then, (14) is obtained by the triangle inequality.

To estimate $\|p-p_h\|_0$, note that $(p-p_h,\operatorname{div} v)=(e_p,\operatorname{div} v)$ for $v\in V_h$ owing to $(p-P_hp,\operatorname{div} v)=0$ by definition of P_h . By (A1), there exists $\boldsymbol{w}\in H^1(\Omega;\mathbb{R}^n)$ such that $\operatorname{div}\boldsymbol{w}=e_p, \|\boldsymbol{w}\|_1\leq C\|e_p\|_0, \ \boldsymbol{w}|_{\Gamma}=0$. Then $\boldsymbol{v}=\Pi_h\boldsymbol{w}\in V_h$ satisfies

$$\operatorname{div} \boldsymbol{v} = \boldsymbol{e}_{p}, \qquad \|\boldsymbol{v}\|_{\operatorname{div}} \lesssim \|\boldsymbol{e}_{p}\|_{\Omega}, \qquad \boldsymbol{v} \cdot \boldsymbol{n}|_{\Gamma} = 0, \tag{17}$$

thanks to (13). Taking this v in (12a), we have

$$\|e_p\|_0^2 = (\kappa^{-1}(\mathbf{u} - \mathbf{u}_h), \mathbf{v}) \le C \|\mathbf{u} - \mathbf{u}_h\|_0 \|\mathbf{v}\|_0 \le C \|\mathbf{u} - \mathbf{u}_h\|_0 \|e_p\|_0$$

As a consequence,

$$\left\| e_p \right\|_0 \leq \begin{cases} C h^{k-1/2} \| \boldsymbol{u} \|_k & \text{if } \boldsymbol{V}_h \text{ is RTN element} \\ C h^{k+1/2} \| \boldsymbol{u} \|_{k+1} & \text{if } \boldsymbol{V}_h \text{ is BDM element} \end{cases}$$

In this estimate, the convergence order of $\left\|e_p\right\|_0$ is 1/2 order superconvergent if the BDM element is used. Finally, (15) is obtained by the triangle inequality. \square

3.2. Improved error analysis

In this subsection we show an improved error analysis under additional assumptions on t_f . Recall that a function g on a domain D is in $W^{1,\infty}(D)$ if g is differentiable in the sense of distributions on D and the derivative of g is in $L^\infty(D)$. For more details on $W^{1,\infty}$ we refer to standard references, e.g., [20,21]. We say that t_f is element-wise $W^{1,\infty}$ on Γ if $t_f|_e \in W^{1,\infty}(e)$ for all $e \in \mathcal{E}_h^\Gamma$, and $\left\|t_f\right\|_{W_h^{1,\infty}(\Gamma)} := \max_{e \in \mathcal{E}_h^\Gamma} \left\|t_f\right\|_e \left\|_{W^{1,\infty}}$.

Let $\overline{t_f}$ be the piecewise constant function on Γ such that $\overline{t_f}|_e$ is the mean value of t_f on $e \in \mathcal{E}_b^{\Gamma}$.

Theorem 4. Assume that t_f is element-wise $W^{1,\infty}$ on Γ . Then,

$$\left\|\kappa^{-1/2}(\boldsymbol{u}-\boldsymbol{u}_h)\right\|_{0} \leq \begin{cases} Ch^{k} \|\boldsymbol{u}\|_{k} & \text{if } \boldsymbol{V}_h \text{ is RTN element} \\ Ch^{k+1} \|\boldsymbol{u}\|_{k+1} & \text{if } \boldsymbol{V}_h \text{ is BDM element} \end{cases}$$
(18)

and

$$||p - p_h||_0 \le Ch^k (||\mathbf{u}||_k + ||p||_k).$$
 (19)

Proof. Let P_h^{Γ} be the L^2 projection to the space

$$\Lambda_h := \{ \lambda \in L^2(\Gamma) : \lambda|_e \in \mathcal{P}_l(e) \quad \forall e \in \mathcal{F}_h \}$$

with l=k if \boldsymbol{V}_h is a BDM element and l=k-1 if \boldsymbol{V}_h is an RTN element. From the definition of Π_h one can see $\Pi_h \boldsymbol{u} \cdot \boldsymbol{n}|_e = P_h^\Gamma(\boldsymbol{u} \cdot \boldsymbol{n})|_e$ for all $e \in \mathcal{F}_h$. Then

$$\left\langle t_f(\mathbf{u} - \Pi_h \mathbf{u}) \cdot \mathbf{n}, e_{\mathbf{u}} \cdot \mathbf{n} \right\rangle_{\Gamma} = \left\langle (t_f - \overline{t_f})(\mathbf{u} - \Pi_h \mathbf{u}) \cdot \mathbf{n}, e_{\mathbf{u}} \cdot \mathbf{n} \right\rangle_{\Gamma}. \tag{20}$$

Applying the Hölder, the Cauchy–Schwarz inequalities, and the Bramble–Hilbert lemma to (20) gives

$$|\left\langle t_{f}(\boldsymbol{u} - \boldsymbol{\Pi}_{h}\boldsymbol{u}) \cdot \boldsymbol{n}, e_{\boldsymbol{u}} \cdot \boldsymbol{n} \right\rangle_{\Gamma}|$$

$$\leq Ch \left\| t_{f} \right\|_{W_{s}^{1,\infty}(\Gamma)} \left\| (\boldsymbol{u} - \boldsymbol{\Pi}_{h}\boldsymbol{u}) \cdot \boldsymbol{n} \right\|_{0,\Gamma} \left\| e_{\boldsymbol{u}} \cdot \boldsymbol{n} \right\|_{0,\Gamma}. \tag{21}$$

If we use the above inequality in (16), then the Cauchy–Schwarz inequality gives

$$\begin{split} \left\| \kappa^{-1/2} e_{\boldsymbol{u}} \right\|_{0} + \left\| t_{f}^{1/2} e_{\boldsymbol{u}} \cdot \boldsymbol{n} \right\|_{0,\Gamma} \\ & \leq C \left(\left\| \kappa^{-1/2} (\boldsymbol{u} - \Pi_{h} \boldsymbol{u}) \right\|_{0} + h \left\| t_{f} \right\|_{W_{h}^{1,\infty}} \left\| (\boldsymbol{u} - \Pi_{h} \boldsymbol{u}) \cdot \boldsymbol{n} \right\|_{0,\Gamma} \right) \end{split}$$
(22)

with a constant C>0 depending on $\|t_f^{-1}\|_{L^\infty(\Gamma)}$. From this and the triangle inequality we have an improved estimate

$$\left\|\kappa^{-1/2}(\boldsymbol{u}-\boldsymbol{u}_h)\right\|_0 \leq \begin{cases} Ch^k \|\boldsymbol{u}\|_k & \text{if } \boldsymbol{V}_h \text{ is RTN element} \\ Ch^{k+1} \|\boldsymbol{u}\|_{k+1} & \text{if } \boldsymbol{V}_h \text{ is BDM element} \end{cases} \tag{23}$$

To estimate $\|p-p_h\|_0$ we take $v \in V_h$ satisfying (17) in (12a), then we have

$$\|e_p\|_0^2 = (\kappa^{-1}(\boldsymbol{u} - \boldsymbol{u}_h), \boldsymbol{v}) \le C \|\boldsymbol{u} - \boldsymbol{u}_h\|_0 \|\boldsymbol{v}\|_0 \le C \|\boldsymbol{u} - \boldsymbol{u}_h\|_0 \|e_p\|_0.$$

As a consequence,

$$\left\| e_p \right\|_0 \leq \begin{cases} Ch^k \left\| \boldsymbol{u} \right\|_k & \text{if } \boldsymbol{V}_h \text{ is RTN element} \\ Ch^{k+1} \left\| \boldsymbol{u} \right\|_{k+1} & \text{if } \boldsymbol{V}_h \text{ is BDM element} \end{cases}$$

In this estimate, the convergence order of $\left\|e_p\right\|_0$ is one order superconvergent if the BDM element is used. Finally, (19) is obtained by the triangle inequality. \square

4. Inversion of transmissibility

In this section we present a statistical inversion of t_f . We start with a Bayesian formulation, prove its well-posedness, present and analyze FEM discretizations of both the state and the parameters, and rigorously establish the convergence of an FEM approximation of the Bayesian posterior measure. We conclude the section with the existence of the maximum a posteriori (MAP) point. A Gaussian approximation of the posterior at the MAP point is also discussed.

4.1. Bayesian inversion on infinite dimensional parameter space

Since t_f is positive on Γ we can define $t_f = e^m$ for $m \in L^2(\Gamma)$. We choose to solve the inverse transmissibility problem using the Bayesian framework as it allows us to account for uncertainties. We assume that there is no model error and thus only uncertainties due to limited noisy data and prior knowledge are taken into account. The Bayesian framework starts with a prior distribution $\mu_{\rm pr}$ of the parameter field m and then update it to the posterior distribution $\mu_{\rm post}$ using information from observational data γ_d by the Bayes' rule

$$\frac{d\mu_{\text{post}}}{d\mu_{\text{pr}}} \propto \pi_{\text{like}}(y_d|m) \tag{24}$$

where $d\mu_{\rm post}/d\mu_{\rm pr}$ is the Radon–Nikodym derivative of the posterior measure $\mu_{\rm post}$ with respect to the prior measure $\mu_{\rm pr}$, and $\pi_{\rm like}(y_d|m)$ is the likelihood according to the data y_d .

To show that (24) is well-posed, we postulate the prior distribution of m as a Gaussian measure in $L^2(\Gamma)$, i.e., $\mu_{\rm pr} = \mathcal{N}(m_{\rm pr}, C_{\rm pr})$, where $m_{\rm pr}$ resides in the Cameron-Martin space \mathcal{M} of $C_{\rm pr}$. It is sufficient for the prior Gaussian measure to be well-defined if we choose $C_{\rm pr} = (\delta I - \gamma \Delta)^{-\sigma}$ for $\sigma > (n-1)/2$ with constants $\delta, \gamma > 0$ [22,23], where we have assumed that Γ is piecewise linear so that the standard Laplacian operator Δ is meaningful. In this case, the parameter m, distributed under the prior $\mu_{\rm pr}$, is almost surely r-Hölder continuous on Γ for any $0 < r < \min\{1, \sigma - (n-1)/2\}$, i.e., $m \in C^{0,r}(\Gamma)$, and almost surely in $H^r(\Gamma)$ for $0 \le r < \sigma - (n-1)/2$. By forcing the domain of $\delta I - \gamma \Delta$ to consist of functions having homogeneous Dirichlet and/or Neumann boundary conditions, we can show that the Cameron-Martin space is $\mathcal{M} = H^\sigma(\Gamma)$.

For the likelihood, we adopt the additive noise model

$$v_d = \mathcal{F}(m) + \eta \tag{25}$$

where $\mathcal{F}: L^2(\Gamma) \mapsto \mathbb{R}^{n_{obs}}$ is the parameter to observable map and the noise η follows a Gaussian distribution $\mathcal{N}(0,\Gamma_{\text{noise}})$. For a fixed radius R>0 the local average operator of a function g at a point x is defined by

$$\operatorname{avg}_{X}(g) := \frac{1}{|b(x,R)|} \int_{b(x,R)} g(y) \, dy, \tag{26}$$

where b(x,r) is the ball of radius R centered at x. Note that though R can have any finite value, its practical value is problem-dependent and must be chosen with care. In the numerical results of section 5 in which we know a priori that solutions are continuous in certain parts of the domain, we take pointwise measurements for convenience and this corresponds to R=0. The observation operator B is defined by the linear operator $B: Q \to \mathbb{R}^{n_{obs}}$ which takes the local average of pressure at n_{obs} points in Ω (with given $0 < R \ll 1$)

$$\mathcal{F}(m) := Bp(m), \tag{27}$$

where p(m) solves (4) with $t_f = e^m$. In this case the likelihood has a form

$$\pi_{\text{like}}(y_d|m) \propto \exp\left(-\frac{1}{2} \|\mathcal{F}(m) - y_d\|_{\Gamma_{\text{noise}}^{-1}}^2\right).$$

Lemma 1. The Radon-Nikodym derivative in (24) is well-defined in $L^2(\Gamma)$, and the parameter m, under the posterior μ_{post} , almost surely resides in $X:=C^{0,r}(\Gamma)$ for any $0 < r < \min\{1, \sigma - (n-1)/2\}$. Furthermore, the posterior measure is Lipschitz continuous with respect to the data y_d in the Hellinger distance.

Proof. From the definition of the observation operator we have, for any $\varepsilon > 0$ and $m \in X$

$$\begin{split} \|\mathcal{F}(m)\|_{2} & \leq \sqrt{n_{obs}} \max_{i=1,\dots,n_{obs}} \left| \operatorname{avg}_{x_{i}}(p) \right| \leq \frac{\sqrt{n_{obs} |\Omega|}}{|b(0,R)|} \, \|p\|_{0} \\ & \leq \frac{\sqrt{n_{obs} |\Omega|}}{|b(0,R)|} \, \frac{\|a\|}{\beta^{2}} \, \|f\|_{0} \leq \frac{\sqrt{n_{obs} |\Omega|}}{|b(0,R)|} \, \frac{\|f\|_{0}}{\beta^{2}} C(\kappa) e^{\|m\|_{\infty}}, \end{split}$$

where $C(\kappa)$ is a constant depending only on κ and we have used the bounds on $\|p\|_0$ and $\|a\|$ in the proof of Theorem 2. In addition, from Theorem 2, p, as a function of t_f , and hence m, is Lipschitz continuous, and as a result, the forward map is locally Lipschitz continuous in m, i.e.,

$$\left\| \mathcal{F}\left(m^{1}\right) - \mathcal{F}\left(m^{2}\right) \right\|_{2} \leq C \left\| m^{1} - m^{2} \right\|_{X}$$

for some constant C. The well-definedness of the Radon-Nikodym derivative in (24) then follows [22, Theorem 4.1] and the local Lipschitz continuity with respect to the data in the Hellinger distance follows [22, Theorem 4.2]. \square

4.2. Analysis of an FEM approximation of the Bayesian posterior

In this section, we first approximate the forward problem (and hence the likelihood) of the Radon-Nikodym derivative (24) using the mixed FEM presented in section 3. We then approximate the parameter, and hence the prior measure, with a continuous FEM method. We then combine these two approximations to arrive at an FEM approximation of the Bayesian posterior. Rigorous analysis of each approximation will be presented.

4.2.1. Likelihood approximation with mixed FEM

For clarity of the exposition, we consider only the mixed FEM with the BDM elements, since the analysis for the RTN elements follows similarly. We denote by $\mathcal{F}_h(m)$ the observation operator Bp_h where (u_h,p_h) is the solution of (11) with $t_f=e^m$. The following result is a direct consequence of Theorem 3.

Lemma 2. For any R > 0 in (26), and $m \sim \mu_{pr}$, there exists a constant C independent of the mesh size h such that

$$\|\mathcal{F}(m) - \mathcal{F}_h(m)\| \le Ch^k e^{\|m\|_{\infty}}.$$

4.2.2. Prior approximation with continuous FEM

We denote by $m_{h,1}=I_hm$ the discretization (interpolation) of m using the standard C^0 finite element method of degree $k_m\geq 1$ on the triangulation \mathcal{E}_h^Γ of Γ (cf. [18]). Note that due to the low regularity of $m\in C^{0,r}(\Gamma)$, the usual $\mathcal{O}(h^{k_m})$ convergence rate of the FEM interpolation error does not apply here. To obtain such an estimate, we first recall an embedding result of Hölder spaces into Sobolev spaces: for $(s,q),\ s\geq 0$, $1\leq q<\infty$ satisfying (n-1)/q+s=r we have

$$||m||_{W^{s,q}(\Gamma)} \le C||m||_{C^{0,r}(\Gamma)},$$
 (28)

for C > 0 depending only on Γ . By choosing a sufficiently large q, we can take s < r as close to r as we desire. For fixed $0 \le r < \min\{1, \sigma - (n-1)/2)\}$, we can use (28) to conclude that $m \in W^{s,q}(\Gamma)$ for (s,q) satisfying

$$s = r - \frac{\varepsilon}{2}, \quad \frac{n-1}{a} = \frac{\varepsilon}{2},$$

with an arbitrarily small $0 < \varepsilon \ll \min\{1, \sigma - (n-1)/2\}$. For this (ε, s, q) , by [18, Theorem 4.4.20], we have

$$\|m - m_{h,1}\|_{\infty} \le Ch^{s - \frac{n-1}{q}} \|m\|_{W^{s,q}(\Gamma)} = Ch^{r-\varepsilon} \|m\|_{W^{s,q}(\Gamma)}.$$
 (29)

Here, the FEM interpolation order k_m is not involved 3 in this estimate due to r < 1.

The following is a simple application of Theorem 2 to the discrete system (11) together with the error bound (29), Lemma 2, and (28).

Lemma 3. Let p_h and $p_{h,1}$ be the solutions of the discrete system (11) corresponding to m and $m_{h,1}$, respectively. Let $m \sim \mu_{\rm pr}$, and thus $m \in C^{0,r}(\Gamma)$, where $r \in (0, \min\{1, \sigma - (n-1)/2\})$, and $0 < \varepsilon \ll \min\{1, \sigma - (n-1)/2\}$. Then there exists a constant $C = C(\varepsilon)$ independent of the mesh size h but dependent on ε such that

$$\left\|\mathcal{F}_h\left(m\right)-\mathcal{F}_h\left(m_{h,1}\right)\right\|\leq Ch^{r-\varepsilon}e^{\|m\|_{\infty}},$$

and

$$\left\|\mathcal{F}\left(m\right)-\mathcal{F}_{h}\left(m_{h,1}\right)\right\|\leq C\left(h^{r-\varepsilon}+h^{k}\right)e^{\left\|m\right\|_{\infty}}.$$

Since the interpolation I_h is a linear operator on $m \in X$ and $\mu_{\rm pr}$ is Gaussian, $m_{h,1} = I_h m$ is distributed by the pushforward measure $\mu_{\rm pr}^h$ induced by I_h that is also a Gaussian. Let us denote by $\mu_{\rm pr}^\perp$ the complement measure of $\mu_{\rm pr}^h$ in $X := C^{0,r}(\Gamma)$ such that $\mu_{\rm pr} = \mu_{\rm pr}^h \bigotimes \mu_{\rm pr}^\perp$, as this will be useful for the fully discrete Bayes formula presented below.

4.2.3. FEM approximation of the Bayesian posterior

Let us denote by $\mu_{\text{post}}^{h,1}$ the FEM approximation of the posterior measure μ_{post} using the likelihood and prior approximations in sections 4.2.1–4.2.2.

Theorem 5 (Well-posedness and convergence of FEM posterior $\mu_{\text{post}}^{h,1}$). The FEM posterior measure $\mu_{\text{post}}^{h,1}$ is absolutely continuous with respect to the prior measure μ_{pr} and the Radon-Nikodym derivative is given by

$$\frac{d\mu_{\text{post}}^{h,1}}{d\mu_{\text{pr}}} \propto \exp\left(-\frac{1}{2} \|\mathcal{F}_h(m_{h,1}) - y_d\|_{\Gamma_{\text{noise}}^{-1}}^2\right). \tag{30}$$

Furthermore, there hold:

- the FEM posterior measure $\mu_{\mathrm{post}}^{h,1}$ is locally Lipschitz continuous with respect to the data y_d in the Hellinger distance.
- $d_{Hell}\left(\mu_{\mathrm{post}},\mu_{\mathrm{post}}^{h,1}\right) \leq C\left(h^{r-\varepsilon}+h^{k}\right)$, where $d_{Hell}\left(\cdot,\cdot\right)$ is the Hellinger distance and $0 < \varepsilon \ll \min\{1,\sigma-(n-1)/2\}$. Thus, the FEM posterior $\mu_{\mathrm{post}}^{h,1}$ converges to the true posterior measure μ_{post} as the mesh is refined.

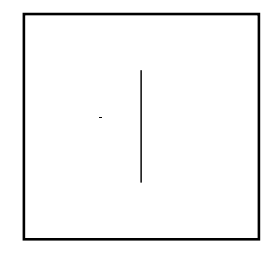
Proof. Similar to Lemma 1, it is sufficient to show that $\mathcal{F}_h(m_{h,1})$ is exponentially bounded in m and locally Lipschitz continuous with respect to m. For the boundedness, we have

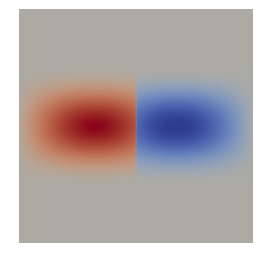
$$\begin{split} \left\| \mathcal{F}_h \left(m_{h,1} \right) \right\|_2 & \leq \frac{\sqrt{n_{obs} \left| \Omega \right|}}{\left| b(0,R) \right|} \left\| p_{h,1} \right\|_0 \leq \frac{\sqrt{n_{obs} \left| \Omega \right|}}{\left| b(0,R) \right|} \frac{\left\| a \right\|}{\beta^2} \left\| f \right\|_0 \\ & \leq \frac{\sqrt{n_{obs} \left| \Omega \right|}}{\left| b(0,R) \right|} \frac{\left\| f \right\|_0}{\beta^2} C(\kappa) e^{\left\| m_{h,1} \right\|_\infty} \leq C \frac{\sqrt{n_{obs} \left| \Omega \right|}}{\left| b(0,R) \right|} \frac{\left\| f \right\|_0}{\beta^2} C(\kappa) e^{\left\| m \right\|_\infty}, \end{split}$$

$$\left\| m - m_{h,1} \right\|_{\infty} \leq C h^{s - \frac{n-1}{2}} \, \left\| m \right\|_{H^{s}(\Gamma)}, \qquad \frac{n-1}{2} < s \leq \min\{r, k_m\},$$

by [18, Theorem 4.4.20].

 $^{^3}$ If $\sigma > (n-1)$, then m resides in $C^{0,r}$ for $0 < r < \min\{1, \sigma - (n-1)/2\}$ and $\|m\|_{\infty} \le C\|m\|_{H^r(\Gamma)}$ for $(n-1)/2 < r < \sigma - (n-1)/2$. In this case, a higher order estimate by polynomials of degree k_m can be obtained as





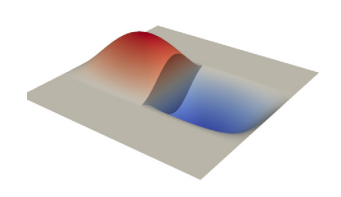


Fig. 2. The domain with a vertical fault in numerical experiments (left figure) and the graphs of the pressure field in (34) (middle and right figures).

where, in the second to last inequality, we used the linearity and the boundedness of the finite element interpolant I_h . For the Lipschitz continuity, Theorem 2 is also valid for p_h , and thus

$$\left\|\mathcal{F}_h\left(m_{h,1}^1\right)-\mathcal{F}_h\left(m_{h,1}^2\right)\right\|\leq C\left\|m_{h,1}^1-m_{h,1}^2\right\|_{\infty}\leq C\left\|m^1-m^2\right\|_{\infty}.\quad \ \Box$$

Now, owing to the fact that $\mu_{pr} = \mu_{pr}^h \bigotimes \mu_{pr}^{\perp}$, $\mu_{post}^{h,1}$ is absolutely continuous with respect to μ_{pr} , and the right hand side of (30) is a function of only $m_{h,1}$, we deduce that $\mu_{post}^{h,1} = \mu_{post}^h \bigotimes \mu_{pr}^{\perp}$, where

$$\frac{d\mu_{\text{post}}^{h}}{d\mu_{\text{pr}}^{h}} \propto \exp\left(-\frac{1}{2}\|\mathcal{F}_{h}(m_{h,1}) - y_{d}\|_{\Gamma_{\text{noise}}^{-1}}^{2}\right)$$
(31)

is a well-defined finite dimensional approximation of the infinite dimensional Bayes formula (24). This expression can then be employed in computations, including the Laplace approximation presented in the next section.

Remark 1. It should be emphasized that $\mu_{\text{post}}^{h,1}$ is the FEM approximation of the posterior measure μ_{post} while μ_{post}^h is the computable part of $\mu_{\text{post}}^{h,1}$. Thus, unlike the forward error analysis presented in sections 3.1–3.2, for which we can verify the convergence rates numerically, it is not trivial to verify the theoretical convergence result via Hellinger distance in Theorem 5 as μ_{pr}^{\perp} —a measure on infinite dimensional space—is not known.

4.3. MAP computation and Laplace approximation

The Maximum a posteriori (MAP) point of μ_{post} is a solution of

$$\underset{m \in \mathcal{M}}{\operatorname{argmin}} \frac{1}{2} \left(\| \mathcal{F}(m) - y_d \|_{\Gamma_{\text{noise}}^{-1}}^2 + \| m - m_{\text{pr}} \|_{\mathcal{M}}^2 \right). \tag{32}$$

The existence of such a MAP point is a direct consequence of the compactness of the Cameron-Martin space \mathcal{M} and the continuity of $\mathcal{F}(m)$.

Therefore the MAP computation can be considered as solving a deterministic inverse problem in which the regularization naturally comes from the prior distribution. When $d\mu_{\rm pr}$ is Gaussian and the PDE model and ${\cal F}$ are linear, then the posterior distribution is not guaranteed to be Gaussian with mean $m_{\rm post}$ and covariance $C_{\rm post}$ of the form

$$m_{\mathrm{post}} = m_{\mathrm{MAP}}, \qquad C_{\mathrm{post}} = (\mathcal{F}^* \Gamma_{\mathrm{noise}}^{-1} \mathcal{F} + C_{\mathrm{pr}}^{-1})^{-1} = \mathcal{H}(m_{\mathrm{MAP}})^{-1}.$$

If the linearity assumptions on the PDE model and $\mathcal F$ are not true, then the posterior distribution is not Gaussian. Nonetheless it is reasonable to expect in many applications that the Laplace approximation $\mathcal N(m_{\rm MAP},\mathcal H(m_{\rm MAP})^{-1})$ is still a good approximation of $\mu_{\rm post}$. An approach to compute the MAP point $m_{\rm MAP}$ efficiently using an inexact Newton method is discussed in Appendix A.

For the Laplace approximation we need to compute $\mathcal{H}(m_{\mathrm{MAP}})^{-1}$ but it is prohibitive to do so explicitly for infinite dimensional parameter spaces because the discretized Hessian is a full matrix, each of whose columns requires a linearized forward PDE solve to construct. For efficient approximation of $\mathcal{H}(m_{\mathrm{MAP}})^{-1}$, we use the definition

$$\mathcal{H}(m_{\text{MAP}})^{-1} = (\mathcal{H}_{\text{misfit}}(m_{\text{MAP}}) + C_{\text{pr}}^{-1})^{-1},$$

where $\mathcal{H}_{\mathrm{misfit}}(m_{\mathrm{MAP}})$ is the Hessian of the misfit $\frac{1}{2}\|\mathcal{F}(m)-y_d\|_{\Gamma^{-1}}^2$ at m_{MAP} . The expected information gain from the data between the prior and the posterior is given (in the linear case) by $\Sigma_i \log(1+\lambda_i)$, where λ_i are the eigenvalues of the *prior-preconditioned data misfit Hessian* $C_{\mathrm{pr}}^{1/2}\mathcal{H}_{\mathrm{misfit}}(m_{\mathrm{MAP}})C_{\mathrm{pr}}^{1/2}$ [23]. Thus, when the eigenvalues decay rapidly as is common for ill-posed inverse problems, the directions in parameter space most informed by the data can be estimated by finding the r eigenvectors of $C_{\mathrm{pr}}^{1/2}\mathcal{H}_{\mathrm{misfit}}(m_{\mathrm{MAP}})C_{\mathrm{pr}}^{1/2}$ corresponding to $\lambda_i > 1$. This allows us to replace $\mathcal{H}_{\mathrm{misfit}}(m_{\mathrm{MAP}})$ by a low-rank approximation with controllable accuracy. The computation of the low-rank approximation can be done independent of the parameter space dimension by randomized singular value decomposition algorithms [24,25] at the cost of r forward/adjoint PDE solves. Then an approximation of $\mathcal{H}(m_{\mathrm{MAP}})^{-1}$ can be computed efficiently using the Sherman–Morrison–Woodbury formula (see, e.g., [23,14] for details).

5. Numerical results

In our numerical experiments we use hIPPYlib [13,14] and FEniCS 2019.1.0 [12].

5.1. Forward problems

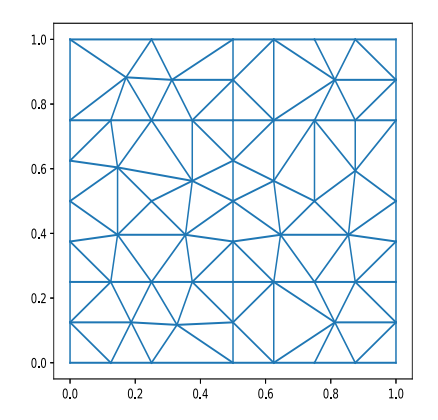
In this subsection we numerically assess the convergence rate of the FEM approximation of the subsurface flow model in faulted domains (forward model). In all numerical experiments below we use the lowest order Raviart–Thomas element and piecewise constant element for \boldsymbol{u} and \boldsymbol{p} , so the expected optimal convergence rates are 1 for \boldsymbol{u} and \boldsymbol{p} if they are in $H^1(\Omega;\mathbb{R}^s)$ and $H^1(\Omega)$. In the first numerical experiment we manufacture a solution that has enough regularity to achieve the expected rate of convergence. In the second numerical experiment we consider a fault geometry of practical interest and a manufactured solution \boldsymbol{u} with the Sobolev regularity only H^s for some s < 1.

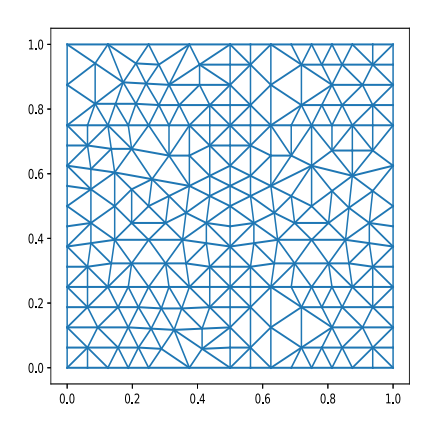
In the first numerical experiment we consider a special manufactured solution with smooth functions on $\mathring{\Omega} := \Omega \setminus \Gamma$. Specifically, on the unit square domain $\Omega = [0,1] \times [0,1]$ with fault $\Gamma = \{(x,y) : x = 1/2\}$, let n, u be

$$p(x,y) = \begin{cases} x^3 & \text{if } x < \frac{1}{2} \\ x^3 + 1 & \text{if } x > \frac{1}{2} \end{cases}, \qquad \mathbf{u}(x,y) = (3x^2, 0).$$
 (33)

Note that ${\bf u}$ can be extended to Γ as a smooth function on Ω , and one can check that $(2{\bf c})$ is satisfied with $t_f=\frac{4}{3}$. Let Γ_L , Γ_R , Γ_T , Γ_B be the left, right, top, and bottom boundary parts of Ω . We impose Dirichlet boundary conditions on $\Gamma_L \cup \Gamma_R$ and Neumann boundary conditions on $\Gamma_T \cup \Gamma_B$ with the manufactured solution. For $f={\rm div}\,{\bf u}$ convergence rates of numerical solutions are obtained in Table 1. Note that t_f satisfies the assumption in Theorem 4, so the results in Table 1 show the expected convergence rates in our error analysis.

In the second numerical experiment we consider a domain $\Omega = [0,1] \times [0,1]$ with fault $\Gamma = \{1/2\} \times [1/4,3/4] \subset \Omega$ (see the left panel of Fig. 2). The manufactured solution (see the middle and right panels of Fig. 2 for its graph) for this test case is given by





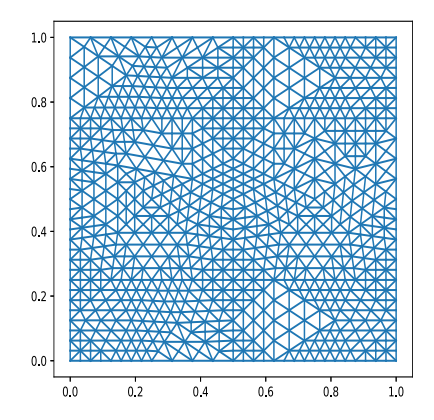


Fig. 3. An unstructured mesh containing the interfaces of 4 subdomains (cf. (35)) in the union of edges, and its two refinements.

Table 1Convergence rates for the example with the manufactured solution (34).

$h_{\rm max}$	$\ \boldsymbol{u}-\boldsymbol{u}_h\ $		$ p-p_h $	
	error	rate	error	rate
0.3750	2.25e-01	-	7.88e-02	-
0.1875	1.13e-01	0.99	3.93e-02	1.00
0.0938	5.67e-02	1.00	1.96e-02	1.00
0.0469	2.84e-02	1.00	9.80e-03	1.00
0.0234	1.42e-02	1.00	4.90e-03	1.00
0.0117	7.10e-03	1.00	2.45e-03	1.00

$$p(x,y) = \begin{cases} 0 & \text{if } y < \frac{1}{4} \text{ or } y > \frac{3}{4} \\ \sin \frac{3\pi x}{2} \cos^2 \left(2\pi \left(y - \frac{1}{2}\right)\right) & \text{if } x < \frac{1}{2} \text{ and } \frac{1}{4} \le y \le \frac{3}{4} \\ -\sin \frac{3\pi (1-x)}{2} \cos^2 \left(2\pi \left(y - \frac{1}{2}\right)\right) & \text{if } x > \frac{1}{2} \text{ and } \frac{1}{4} \le y \le \frac{3}{4}. \end{cases}$$
(34)

Setting $\kappa=1$ we can compute $\mathbf{u}=-\nabla p$ and $f=\operatorname{div}\mathbf{u}$ on $\mathring{\Omega}$. It can be verified by direct computation that limits of the normal component of \mathbf{u} on Γ are continuous across Γ and the condition $t_f\mathbf{u}\cdot\mathbf{n}-[[p]]=0$ holds with $t_f=4/(3\pi)$. However, by computing $\partial p/\partial y$ of p in (34) and taking limits as $x\to \frac{1}{2}^+$ and $x\to \frac{1}{2}^-$, one can check that the tangential component of \mathbf{u} is not continuous on Γ . Therefore, the regularity of \mathbf{u} is lower than $H^1(\Omega;\mathbb{R}^2)$.

By using Γ_L , Γ_R , Γ_T , Γ_B to denote the boundary parts as before, we impose boundary conditions

$$p = 0$$
 on $\Gamma_L \cup \Gamma_R$, $\boldsymbol{u} \cdot \boldsymbol{n} = 0$ on $\Gamma_T \cup \Gamma_B$.

Note that u, p are smooth on the 4 subdomains

$$0 < x < 1, 0 \le y < \frac{1}{4}, \qquad 0 < x < 1, \frac{3}{4} < y < 1,$$
 (35a)

$$0 < x < \frac{1}{2}, \frac{1}{4} < y < \frac{3}{4}, \qquad \frac{1}{2} < x < 1, \frac{1}{4} < y < \frac{3}{4}.$$
 (35b)

A standard approximation theory requires a regularity of exact solutions only on each triangle, not on Ω . Therefore, if the interfaces of these 4 subdomains are in the union of edges of triangulations (see Fig. 3), then we can expect convergence rates of u and p that are optimal for the finite element spaces. For error computation we use $\Pi_h u$ and $P_h p$ of the manufactured solutions, and compute the L^2 norms of the difference of these projected functions and numerical solutions. The errors and convergence rates for the lowest order (k=1) RTN and BDM elements are presented in Table 2 and Table 3.

For convenience of numerical implementation with the manufactured solution (34), we used meshes conforming to the 4 subdomains (35). However, we do not know the 4 subdomains in (35) such that exact solutions are smooth in general, so there is no guarantee that we can find ideal triangulations such that exact solutions are smooth on each triangle. From this point of view, the second order convergence

Table 2Convergence rates for the example with the manufactured solution (34) and the lowest order RTN element.

$h_{\rm max}$	$\ \Pi_h \boldsymbol{u} - \boldsymbol{u}_h\ _0$		$\ P_hp-p_h\ _0$	
	error	rate	error	rate
0.2500	3.32e-01	-	9.67e-02	_
0.1398	8.34e-02	1.99	4.82e-02	1.00
0.0699	2.97e-02	1.49	2.48e-02	0.96
0.0349	1.22e-02	1.28	1.25e-02	0.99
0.0175	5.69e-03	1.10	6.26e-03	1.00
0.0087	2.79e-03	1.03	3.12e-03	1.00

Table 3Convergence rates for the example with the manufactured solution (34) and the lowest order BDM element.

$h_{\rm max}$	$\ \Pi_h \boldsymbol{u} - \boldsymbol{u}_h\ _0$		$\ P_hp-p_h\ _0$	
	error	rate	error	rate
0.2500	3.37e-01	-	1.02e-01	-
0.1398	6.95e-02	2.28	4.90e-02	1.05
0.0699	1.75e-02	1.98	2.49e-02	0.98
0.0349	4.38e-03	2.00	1.25e-02	1.00
0.0175	1.09e-03	2.00	6.26e-03	1.00
0.0087	2.73e-04	2.00	3.12e-03	1.00

rate of $\|\Pi_h \mathbf{u} - \mathbf{u}_h\|_0$ in Table 3 is due to ideal triangulations, and we remark that convergence rates of $\|\Pi_h \mathbf{u} - \mathbf{u}_h\|_0$ with the lowest order BDM elements on general meshes are lower than 2. By direct computation one can verify \mathbf{u} is continuous on the segments y = 1/4 and y = 3/4, and therefore $\mathbf{u} \in H^1(\mathring{\Omega}, \mathbb{R}^2)$. However, the derivatives of \mathbf{u} have discontinuities on y = 1/4 and y = 3/4. Therefore, if the segments y = 1/4 or y = 3/4 split a triangle in a triangulation of Ω , then numerical approximation of exact solutions on such a triangle will not give a second order convergence rate.

5.2. MAP computation as deterministic inverse problem

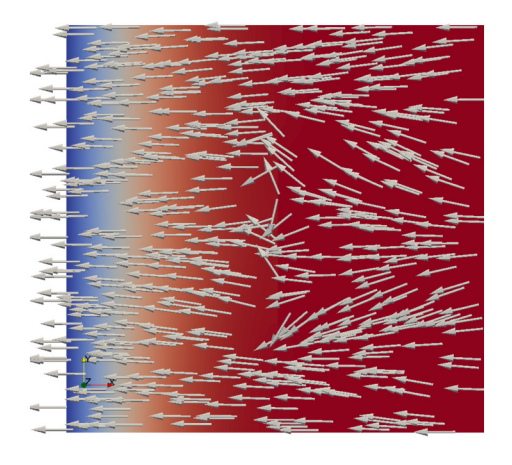
To numerically test the deterministic inverse problem solution, we find the MAP point of the problem (32) using the inexact Newton-CG algorithm in Appendix A. The domain and fault are $\Omega = [0,1] \times [0,1]$, $\Gamma = \{1/2\} \times [1/4,3/4]$, and boundary conditions are

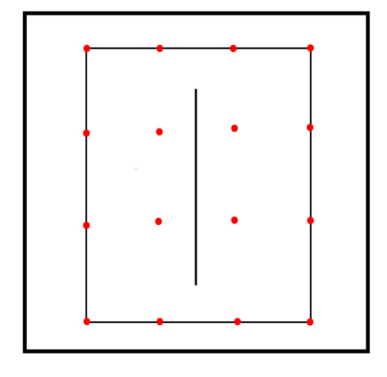
$$p = 0$$
 on Γ_L , $p = 1$ on Γ_R , $\boldsymbol{u} \cdot \boldsymbol{n} = 0$ on $\Gamma_T \cup \Gamma_B$.

We set $\kappa=1$ on Ω and assume that the true transmissibility field on Γ is $t_f=e^m$ with

$$m(y) = 2\sin\left(8\pi\left(y - \frac{1}{2}\right)\right), \qquad \frac{1}{4} \le y \le \frac{3}{4}.$$
 (36)

For the prior we use $C_{\rm pr}=(\delta-\gamma\Delta)^{-1}$ with $\delta=0.4,\ \gamma=0.004$, and $m_{\rm pr}=0$. For the likelihood term, pointwise observations of pressure are





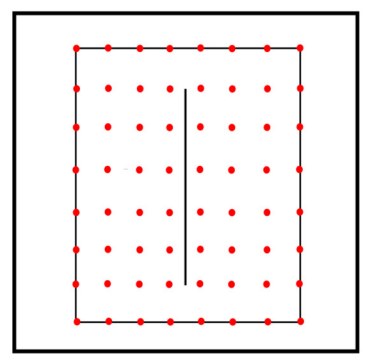


Fig. 4. The pressure and velocity fields with fault parameter $t_f = e^m$ for $m = m_{\text{true}}$ in (36), and 4×4 and 8×8 observation points for fault parameter inversion.

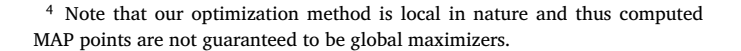
taken at $k \times k$ (k = 4,6,8) uniform lattice points on the observation domain $[0.2,0.8] \times [0.1,0.9]$ as shown in Fig. 4 for the case of 4×4 and 8×8 observation points. We corrupt the observed data vector $\mathbf{d} \in \mathbb{R}^N$, N = 16,36,64, by adding a Gaussian noise vector $\zeta \in \mathbb{R}^N$. Entries of ζ are independent identically distributed and follow a normal distribution $\mathcal{N}(0,\sigma^2)$ with $\sigma = 0.01 \|\mathbf{d}\|_{l^\infty}$. Then, transmissibility inversion by constrained minimization is done with the noisy data $\mathbf{d} + \zeta$.

The approximate MAP points⁴ by deterministic inversion for 4×4 , 6×6 , and 8×8 observation points are shown in Fig. 5. Since 4×4 observations do not provide sufficient information to inform the inverse parameter field, the approximate MAP point is not much different from the prior mean $m\equiv 0$ (also used as the initial guess in our algorithm). Nevertheless, the approximate MAP points with 6×6 and 8×8 observation points capture major features of the true parameter field: clearly it is impossible to capture the true parameter field exactly due to limited and noisy data, the ill-posed nature of the inverse problem, and the smoothing effects of the prior.

5.3. Bayesian inverse problem

We limit ourselves to the Laplace approximation $\mathcal{N}(m_{\mathrm{MAP}}, \mathcal{H}(m_{\mathrm{MAP}})^{-1})$ of the Bayesian inverse problem. A more complete exploration of the Bayesian posterior can be done by standard sampling methods such as Markov chain Monte Carlo methods [26–29]. While such sampling methods provide a full characterization of the discrete finite dimensional posterior (31), they do not provide additional insights or novelties to our work, and thus are not considered.

In the first experiment we consider a simple model with one vertical fault shown in Fig. 4. We first present the dominant eigenvalues of prior-preconditioned Hessian of data misfit $C_{\rm pr}^{1/2}\mathcal{H}_{\rm misfit}(m_{\rm MAP})\mathcal{C}_{\rm pr}^{1/2}$ in



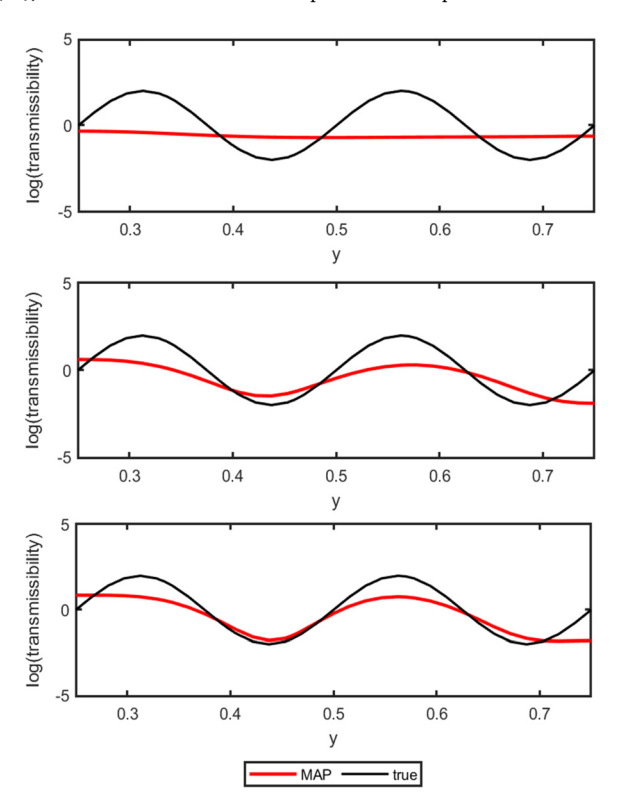


Fig. 5. The $\log(t_f)$ fields of true parameter and approximate MAP points for 4×4 , 6×6 , and 8×8 observation points.

Fig. 6. In the case of 4×4 observations, just two eigenvalues are larger than 1, indicating just two directions in the space of parameters can be inferred from the data with high confidence (the rest are insufficiently

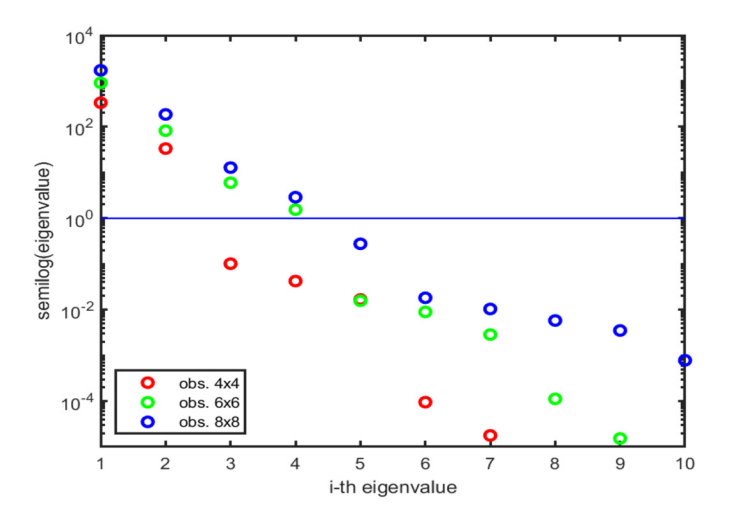


Fig. 6. Eigenvalues of the prior-preconditioned Hessian of the data misfit to different sets of observations.

informed by the data, and are thus dominated by the prior). Moving to 6×6 observations results in a slower decay of eigenvalues, yielding four data-informed parameter directions. Finally, increasing the observations to an 8×8 grid yields further increases in eigenvalues, and thus more information gain, though there are diminishing returns. This allows us to compute the Laplace approximation $\mathcal{N}(m_{\text{MAP}},\mathcal{H}(m_{\text{MAP}})^{-1})$ efficiently with low rank approximation (see, e.g., [30] for more details)

In Fig. 7, we compare the credibility intervals of

$$\mathcal{N}(0, C_{\text{Dr}})$$
 and $\mathcal{N}(m_{\text{MAP}}, \mathcal{H}(m_{\text{MAP}})^{-1})$

for 4×4 observation points. The shaded (yellow) regions denote the union of pointwise credibility intervals with the length $2\sigma_{\rm std}$ where $\sigma_{\rm std}$ are the empirical pointwise variances. We draw 5 random samples from $\mathcal{N}(0,\mathcal{C}_{\rm pr})$ and $\mathcal{N}(m_{\rm MAP},\mathcal{H}(m_{\rm MAP})^{-1})$ and plot them in the corresponding subfigures.

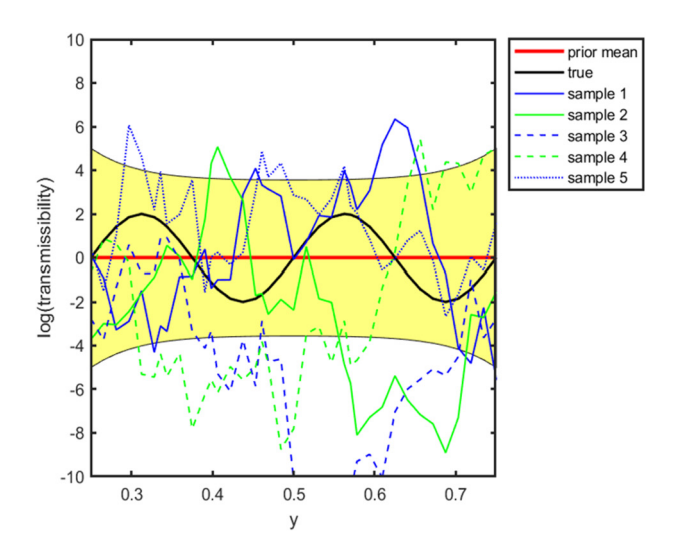
Similarly, Figs. 8 and 9 present pointwise credibility intervals of the prior and the Laplace approximation of the posterior for the cases with with 6×6 and 8×8 observation points, respectively. It is clear that $\mathcal{N}(m_{\text{MAP}}, \mathcal{H}(m_{\text{MAP}})^{-1})$ corresponds to a much narrower credibility region than that of $\mathcal{N}(0, \mathcal{C}_{\text{Dr}})$. This is expected due to observational

data. This in turns significantly reduces the uncertainty in the posterior distribution compared to the prior distribution. We also present 5 samples drawn from $\mathcal{N}(0, C_{\mathrm{pr}})$ and $\mathcal{N}(m_{\mathrm{MAP}}, \mathcal{H}(m_{\mathrm{MAP}})^{-1})$: again those drawn from the Laplace approximation of the posterior are closer to the true parameter field.

In the second numerical experiment we present inverse results for a problem with 3 faults with 6×6 observations in the rectangle $[0.15, 0.85] \times [0.15, 0.85]$ as in Fig. 10. The prior $C_{pr} = (\delta - \gamma \Delta)^{-1}$ with $\delta = 0.4$, $\gamma = 0.004$, and $m_{\rm pr} = 0$ is used for all faults. Observational data are synthetically generated using the same procedure as above, and the Laplace approximations on each fault are computed using low rank approximations. The credibility regions and 5 randomly drawn samples of $\mathcal{N}(0,\mathcal{C}_{\mathrm{pr}})$ and $\mathcal{N}(m_{\mathrm{MAP}},\mathcal{H}(m_{\mathrm{MAP}})^{-1})$ are shown in Fig. 11. This problem is more challenging compared to the one-fault case. As can be seen, the prior mean and samples are very different from the ground truth parameter. With the help of observational data, the posterior results using the Laplace approximation are closer to the ground truth parameter field for each fault. As can be seen, the inversion result for the second fault is better than the others. This is not surprising as the second fault is the longest and is surrounded by the largest number of observation points. In order to obtain better inverse results for faults 1 and 3, more observations are needed. Indeed, Fig. 12 shows that the inverse results, both the MAP and uncertainty estimation, are more accurate with 12×12 observation points.

6. Conclusions

This paper concerns the forward and inverse modeling of subsurface flow in domains with faults. In particular, we consider the inverse problem for fault transmissibility in subsurface flow models under appropriate assumptions on fault structures. We provide a complete and thorough analysis of the transmissibility inverse problem including fault modeling, well-posedness of the forward PDE, FEM discretizations of the forward PDE and their rigorous analysis, well-posedness of the Bayesian inverse formulation, discretizations of Bayesian inverse formulation and their rigorous analysis, and numerical illustrations. We also presented transmissibility inversion problems by a PDE-constrained optimization approach and developed an efficient numerical optimization method utilizing the efficient computation of Hessian action via Lagrangian approach. The results show that our approach can provide reasonable inverse solutions together with their associated uncertainty estimation. Ongoing work is to extend our framework to problem with more realistic networks of faults and three dimensional problems.



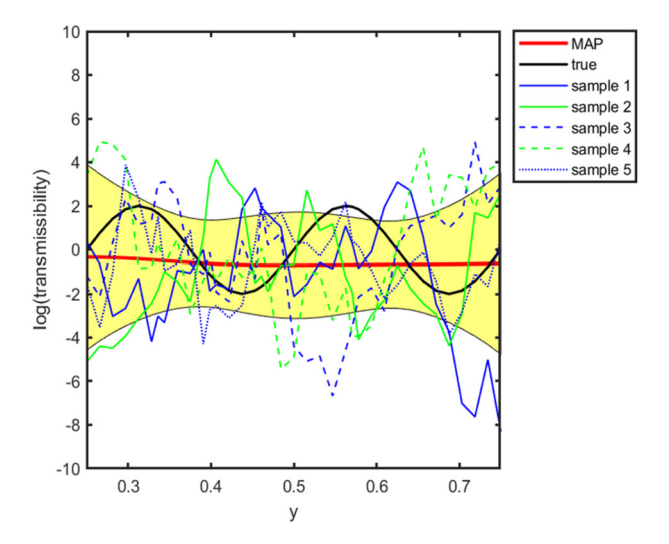
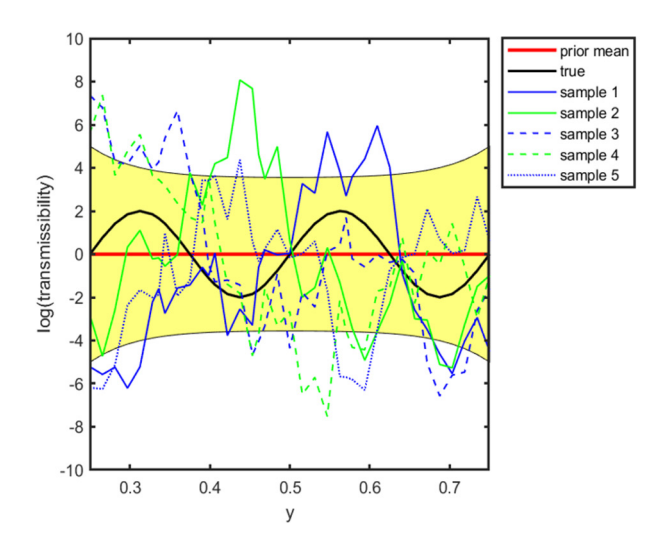


Fig. 7. The comparison of pointwise credibility interval, mean, and samples with $\mathcal{N}(0, C_{pr})$ and the Laplace approximation $\mathcal{N}(m_{MAP}, \mathcal{H}(m_{MAP})^{-1})$ with 4×4 observation points. Left is for the prior and right for the Laplace approximation.



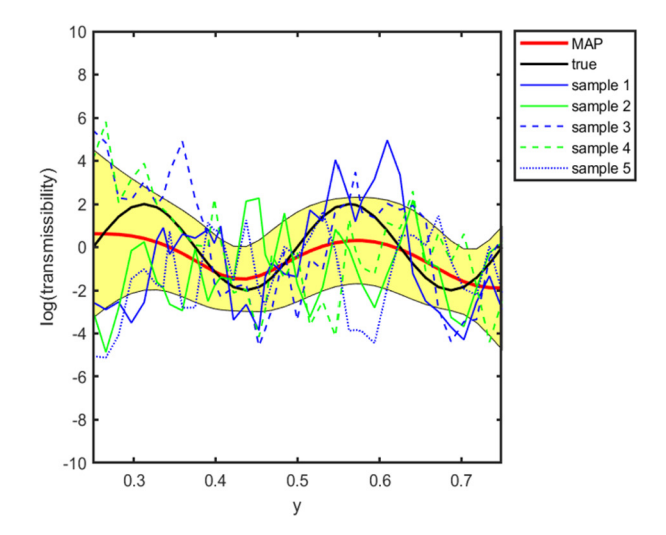
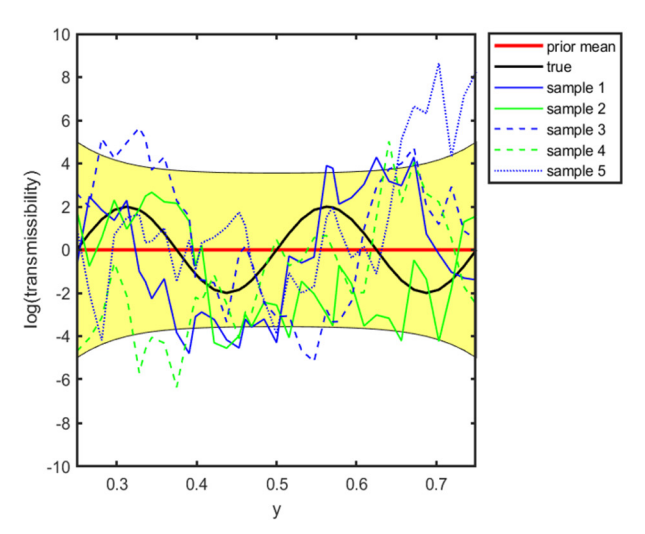


Fig. 8. The comparison of pointwise credibility interval, mean, and samples with $\mathcal{N}(0, C_{pr})$ and the Laplace approximation $\mathcal{N}(m_{MAP}, \mathcal{H}(m_{MAP})^{-1})$ with 6×6 observation points. Left is for the prior and right for the Laplace approximation.



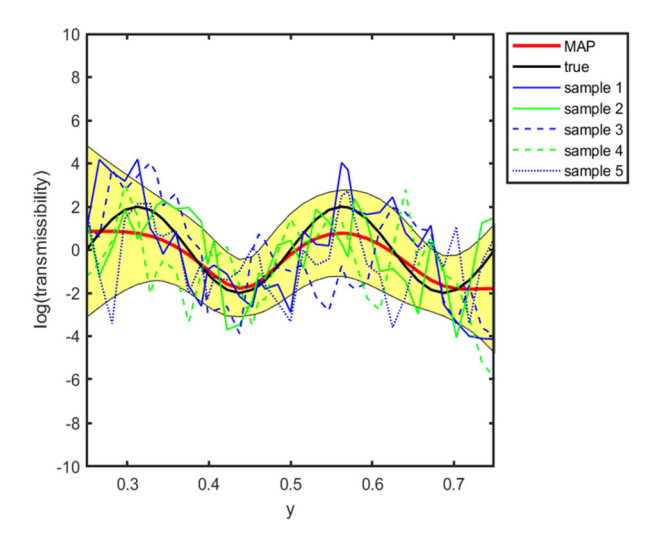


Fig. 9. The comparison of pointwise credibility interval, mean, and samples with $\mathcal{N}(0, C_{pr})$ and the Laplace approximation $\mathcal{N}(m_{MAP}, \mathcal{H}(m_{MAP})^{-1})$ with 8×8 observation points. Left is for the prior and right for the Laplace approximation.

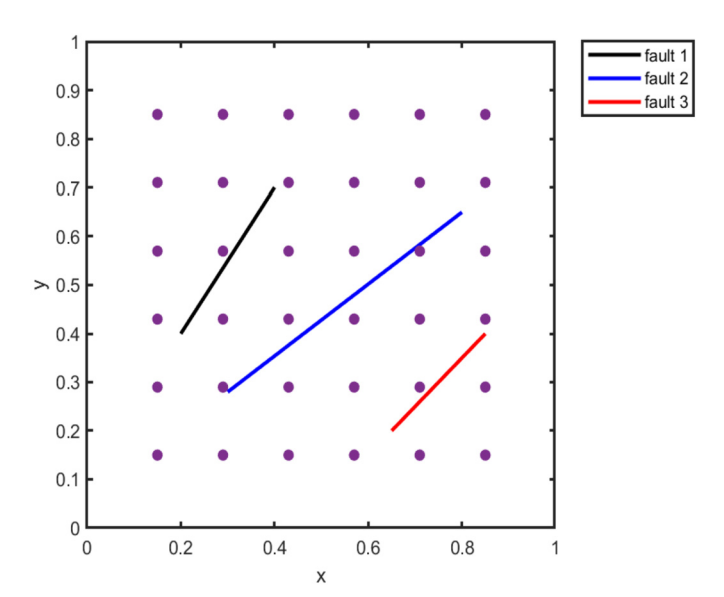


Fig. 10. A domain with three faults and observation points.

Data availability

No data was used for the research described in the article.

Appendix A. MAP computation with an inexact Newton method

Below we present an inexact Newton-Conjugate Gradient (Newton-CG) approach to compute the map point. For concreteness, we consider n=2, and it is sufficient to take $\sigma=1$ for the Gaussian prior to be well-defined. In this case the Cameron-Martin space is $\mathcal{M}=H^1(\Gamma)$ (in fact an equivalence of $H^1(\Gamma)$ with δ and γ as weights: see the definition $\mathcal J$ below). Then the MAP problem becomes the following: solve

 $\mathop{\rm argmin}_{m \in \mathcal{M}} \mathcal{J}(m)$

with

$$\begin{split} \mathcal{J}(m) := & \frac{1}{2} \left(\left\| Bp - y_d \right\|_{\Gamma_{\text{noise}}^{-1}}^2 + \left(\left\langle \delta(m - \bar{m}), (m - \bar{m}) \right\rangle_{\Gamma} \right) \right) \\ & + \frac{1}{2} \left\langle \gamma \nabla(m - \bar{m}), \nabla(m - \bar{m}) \right\rangle_{\Gamma} \end{split}$$

where (u, p) is the solution of forward equation

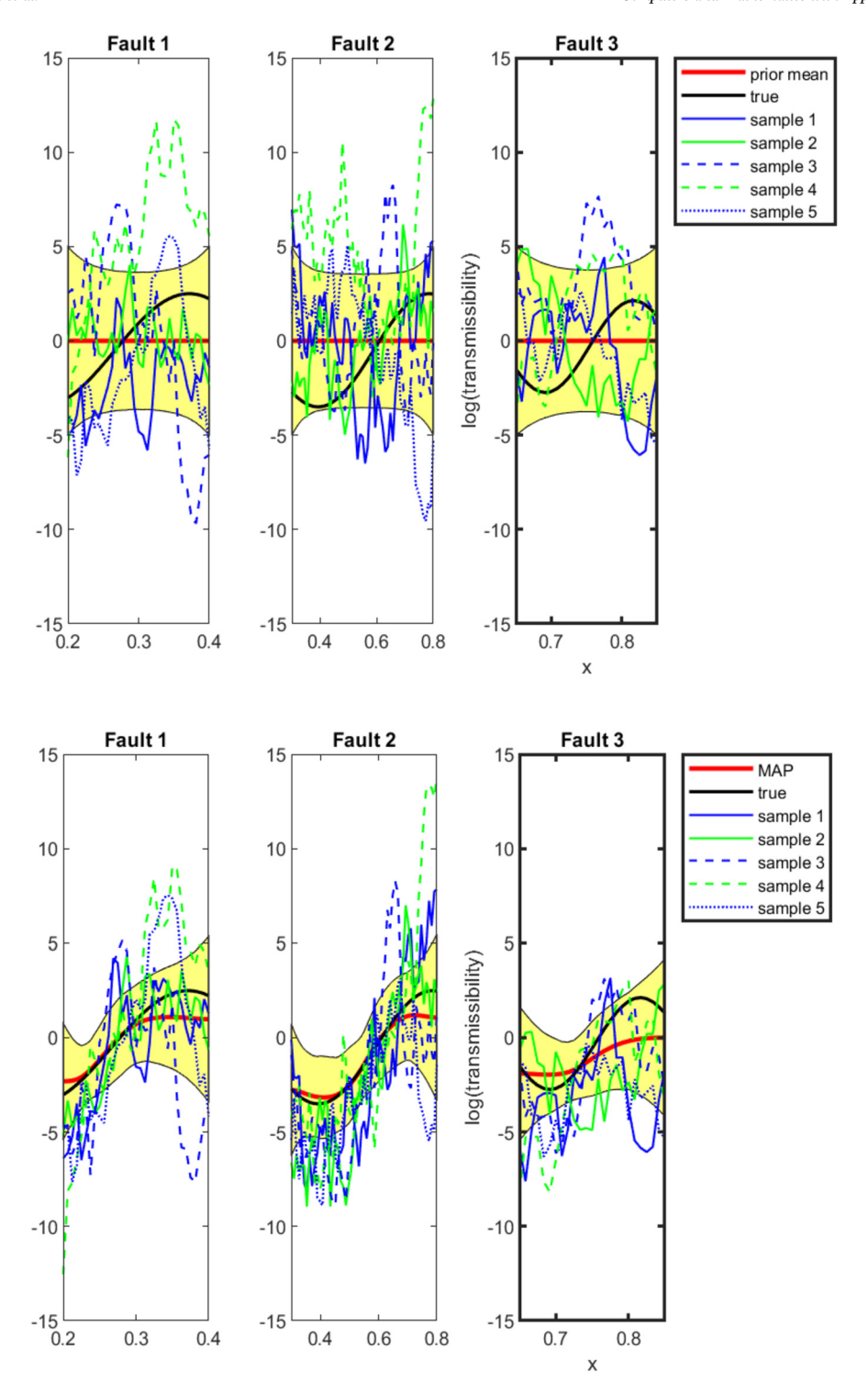


Fig. 11. The comparison of pointwise credibility interval, mean, and samples with $\mathcal{N}(0, C_{pr})$ and the Laplace approximation $\mathcal{N}(m_{MAP}, \mathcal{H}(m_{MAP})^{-1})$ with 6×6 observation points for the problem with three faults. The top row is for the prior and the bottom one is for the posterior using the Laplace approximation.

$$(\kappa^{-1}\mathbf{u}, \mathbf{v}) + \langle e^{m}\mathbf{u} \cdot \mathbf{n}, \mathbf{v} \cdot \mathbf{n} \rangle - (p, \operatorname{div} \mathbf{v}) = 0, \qquad \mathbf{v} \in \mathbf{V},$$

$$(\operatorname{div} \mathbf{u}, q) = (f, q) \qquad q \in Q.$$
(A.1a)

We solve this problem using inexact Newton-type methods with the gradient and Hessian-vector project as in [30]. To compute the gradient of $\mathcal{J}(m)$ we use the Lagrangian functional

$$\begin{split} \mathcal{L}^{\mathcal{G}}((\boldsymbol{u},p),m,(\boldsymbol{v},q)) \\ &= \mathcal{J}(m) + \left(\kappa^{-1}\boldsymbol{u},\boldsymbol{v}\right) + \left\langle e^{m}\boldsymbol{u}\cdot\boldsymbol{n},\boldsymbol{v}\cdot\boldsymbol{n}\right\rangle_{\Gamma} - (p,\operatorname{div}\boldsymbol{v}) + (\operatorname{div}\boldsymbol{u},q) - (f,q), \end{split}$$

with $(u, p), (v, q) \in V \times Q$. The Lagrangian approach for the gradient computation at $m = m_0$ leads to the forward equation (A.1) and the adjoint problem: finding $(v_0, q_0) \in V \times Q$ such that for all $(\tilde{u}, \tilde{p}) \in V \times Q$

$$\begin{split} \langle B\tilde{p},Bp_0-y_d\rangle_{\Gamma_{\text{noise}}^{-1}} + \left(\kappa^{-1}\tilde{\pmb{u}},\pmb{v}_0\right) + \langle e^m\tilde{\pmb{u}}\cdot\pmb{n},\pmb{v}_0\cdot\pmb{n}\rangle_{\Gamma} - \left(\tilde{p},\operatorname{div}\pmb{v}_0\right) \\ + \left(\operatorname{div}\tilde{\pmb{u}},q_0\right) = 0, \quad (A.2) \end{split}$$

where (u_0, p_0) is the forward solution obtained from (A.1) for $m = m_0$. Then the gradient of $\mathcal{J}(m)$ at $m = m_0$ in weak form is: for any $\tilde{m} \in \mathcal{M}$

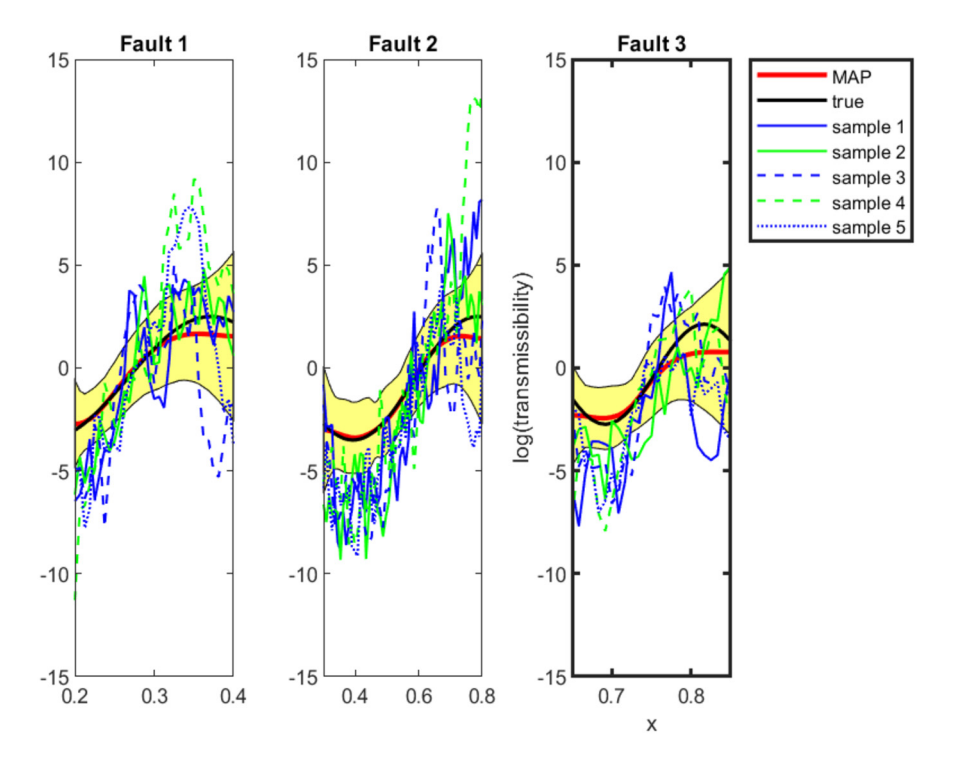


Fig. 12. The credibility interval, mean, and samples with the Laplace approximation $\mathcal{N}(m_{\text{MAP}}, \mathcal{H}(m_{\text{MAP}})^{-1})$ obtained with 12×12 observation points for the problem with three faults.

$$(\mathcal{G}(m_0), \tilde{m}) = \frac{1}{2} \left(\langle \delta(m_0 - \tilde{m}), \tilde{m} \rangle_{\Gamma} + \langle \gamma \nabla m_0, \nabla \tilde{m} \rangle_{\Gamma} \right) + \langle \tilde{m} e^{m_0} \mathbf{u}_0 \cdot \mathbf{n}, \mathbf{v}_0 \cdot \mathbf{n} \rangle_{\Gamma}.$$

For the Hessian-vector product we define $\mathcal{L}^{\mathcal{H}}$ as

$$\begin{split} &\mathcal{L}^{\mathcal{H}}\left((\boldsymbol{u},\boldsymbol{p}),\boldsymbol{m},(\boldsymbol{v},\boldsymbol{q});(\hat{\boldsymbol{u}},\hat{\boldsymbol{p}}),\hat{\boldsymbol{m}},(\hat{\boldsymbol{v}},\hat{\boldsymbol{q}})\right) \\ &= \left(\mathcal{G}(\boldsymbol{m}),\hat{\boldsymbol{m}}\right) + \left\langle \kappa^{-1}\boldsymbol{u},\hat{\boldsymbol{v}}\right\rangle + \left\langle e^{\boldsymbol{m}}\boldsymbol{u}\cdot\boldsymbol{n},\hat{\boldsymbol{v}}\cdot\boldsymbol{n}\right\rangle - \left(\boldsymbol{p},\operatorname{div}\hat{\boldsymbol{v}}\right) + \left(\operatorname{div}\boldsymbol{u},\hat{\boldsymbol{q}}\right) - \left(\boldsymbol{f},\hat{\boldsymbol{q}}\right) \\ &+ \left\langle B\hat{\boldsymbol{p}},B\boldsymbol{p}-\boldsymbol{y}_{\boldsymbol{d}}\right\rangle_{\Gamma^{-1}_{-1}} + \left(\kappa^{-1}\hat{\boldsymbol{u}},\boldsymbol{v}\right) + \left\langle e^{\boldsymbol{m}}\hat{\boldsymbol{u}}\cdot\boldsymbol{n},\boldsymbol{v}\cdot\boldsymbol{n}\right\rangle_{\Gamma} - \left(\hat{\boldsymbol{p}},\operatorname{div}\boldsymbol{v}\right) + \left(\operatorname{div}\hat{\boldsymbol{u}},\boldsymbol{q}\right). \end{split}$$

The variational forms of the incremental forward (finding (\hat{u}, \hat{p})) and incremental adjoint (finding (\hat{v}, \hat{q})) equations are

$$\begin{split} & \left(\kappa^{-1}\hat{\boldsymbol{u}},\tilde{\boldsymbol{v}}\right) + \left\langle e^{m}\hat{\boldsymbol{u}}\cdot\boldsymbol{n},\tilde{\boldsymbol{v}}\cdot\boldsymbol{n}\right\rangle_{\Gamma} - (\hat{p},\operatorname{div}\tilde{\boldsymbol{v}}) \\ & - (\operatorname{div}\hat{\boldsymbol{v}},\tilde{q}) + \left\langle e^{m}\hat{\boldsymbol{m}}\boldsymbol{u}\cdot\boldsymbol{n},\tilde{\boldsymbol{v}}\cdot\boldsymbol{n}\right\rangle_{\Gamma} = 0 \quad \forall (\tilde{\boldsymbol{v}},\tilde{q}), \quad (\operatorname{Inc. Fwd.}) \\ & \left\langle B\tilde{p},B\hat{p}\right\rangle_{\Gamma^{-1}_{\operatorname{noise}}} + (\kappa^{-1}\tilde{\boldsymbol{u}},\hat{\boldsymbol{v}}) + \left\langle e^{m}\tilde{\boldsymbol{u}}\cdot\boldsymbol{n},\hat{\boldsymbol{v}}\cdot\boldsymbol{n}\right\rangle_{\Gamma} - (\tilde{p},\operatorname{div}\hat{\boldsymbol{v}}) \\ & - (\operatorname{div}\tilde{\boldsymbol{u}},\hat{q}) - \left\langle e^{m}\hat{\boldsymbol{m}}\tilde{\boldsymbol{u}}\cdot\boldsymbol{n},\boldsymbol{v}\cdot\boldsymbol{n}\right\rangle_{\Gamma} = 0 \quad \forall (\tilde{\boldsymbol{u}},\tilde{\boldsymbol{p}}). \quad (\operatorname{Inc. Adj.}) \end{split}$$

For $\mathcal{H}(m_0)$, the Hessian of \mathcal{J} evaluated at $m=m_0$, the action of $\mathcal{H}(m_0)$ on $\hat{m} \in \mathcal{M}$ can be written in weak form as

$$\begin{split} \left(\tilde{m}, \mathcal{H}(m_0)\hat{m}\right) &= \left\langle \delta\hat{m}, \tilde{m}\right\rangle_{\Gamma} + \left\langle \gamma\nabla\hat{m}, \nabla\tilde{m}\right\rangle_{\Gamma} + \left\langle \tilde{m}\hat{m}e^{m_0}u_0 \cdot \boldsymbol{n}, \boldsymbol{v}_0 \cdot \boldsymbol{n}\right\rangle_{\Gamma} \\ &+ \left(\kappa^{-1}u_0, \hat{\boldsymbol{v}}\right) + \left\langle \tilde{m}e^{m_0}u_0 \cdot \boldsymbol{n}, \hat{\boldsymbol{v}} \cdot \boldsymbol{n}\right\rangle_{\Gamma} \\ &- \left(p_0, \operatorname{div}\hat{\boldsymbol{v}}\right) + \left(\operatorname{div}u_0, \hat{q}\right) - (f, \hat{q}) \\ &+ \left\langle \tilde{m}e^{m_0}\hat{\boldsymbol{u}} \cdot \boldsymbol{n}, \boldsymbol{v}_0 \cdot \boldsymbol{n}\right\rangle_{\Gamma} \quad \forall \tilde{m} \in \mathcal{M}. \end{split}$$

Based on the gradient and the Hessian action computation algorithms, the maximum a posteriori (MAP) point can be found by a standard Newton method. For efficient performance of Newton methods an inexact Newton-CG algorithm can be used. In the inexact Newton-CG algorithm the system $\mathcal{H}(m_k)\delta_k = -\mathcal{G}(m_k)$ is solved by a preconditioned CG method with early termination of CG iterations using the Eisenstat–Walker criterion and the Steihaug criterion (to prevent oversolving) and the backtracking algorithm (to avoid negative curvature) (see, e.g., [31,14]).

References

- P.M. Adler, J.-F. Thovert, V.V. Mourzenko, Fractured Porous Media, Oxford University Press, Oxford, 2013.
- [2] M. Sahimi, Flow and Transport in Porous Media and Fractured Rock: From Classical Methods to Modern Approaches, John Wiley & Sons, 2nd edition, 2011.
- [3] Z. Chen, G. Huan, Y. Ma, Computational Methods for Multiphase Flows in Porous Media, Computational Science & Engineering, vol. 2, Society for Industrial and Applied Mathematics (SIAM), Philadelphia, PA, 2006.
- [4] K.-A. Lie, An Introduction to Reservoir Simulation Using MATLAB/GNU Octave: User Guide for the MATLAB Reservoir, Simulation Toolbox (MRST), Cambridge University Press, 2019.
- [5] I. Berre, F. Doster, E. Keilegavlen, Flow in fractured porous media: a review of conceptual models and discretization approaches, Transp. Porous Media 130 (2019) 215–236, https://doi.org/10.1007/s11242-018-1171-6.
- [6] V. Martin, J. Jaffré, J.E. Roberts, Modeling fractures and barriers as interfaces for flow in porous media, SIAM J. Sci. Comput. 26 (5) (2005) 1667–1691, https:// doi.org/10.1137/S1064827503429363.
- [7] P. Angot, F. Boyer, F. Hubert, Asymptotic and numerical modelling of flows in fractured porous media, M2AN, Math. Model. Numer. Anal. 43 (2) (2009) 239–275, https://doi.org/10.1051/m2an/2008052.
- [8] E. Ahmed, J. Jaffré, J.E. Roberts, A reduced fracture model for two-phase flow with different rock types, in: mAMERN VI-2015: 6th International Conference on Approximation Methods and Numerical Modeling in Environment and Natural Resources, Math. Comput. Simul. 137 (2017) 49–70, https://doi.org/10.1016/j.matcom.2016. 10.005, https://www.sciencedirect.com/science/article/pii/S0378475416301987.
- [9] H.M. Nilsen, J.R. Natvig, K.-A. Lie, Accurate modeling of faults by multipoint, mimetic, and mixed methods, SPE J. 17 (2) (2012) 568–579, https://doi.org/10. 2118/149690-PA.
- [10] P.F. Antonietti, L. Formaggia, A. Scotti, M. Verani, N. Verzott, Mimetic finite difference approximation of flows in fractured porous media, ESAIM: Math. Model. Numer. Anal. 50 (3) (2016) 809–832, https://doi.org/10.1051/m2an/2015087.
- [11] Website, http://fenicsproject.org/.
- [12] A. Logg, K.-A. Mardal, G.N. Wells (Eds.), Automated Solution of Differential Equations by the Finite Element Method, Lecture Notes in Computational Science and Engineering, vol. 84, Springer, Heidelberg, 2012.
- [13] U. Villa, N. Petra, O. Ghattas, HIPPYlib: an extensible software framework for large-scale deterministic and Bayesian inverse problems, J. Open Sour. Softw. 3 (30) (2018), https://doi.org/10.21105/joss.00940.
- [14] U. Villa, N. Petra, O. Ghattas HIPPYlib, An extensible software framework for large-scale inverse problems governed by PDEs: part I: deterministic inversion and linearized Bayesian inference, ACM Trans. Math. Softw. 47 (2) (Apr. 2021), https://doi.org/10.1145/3428447.

- [15] V. Girault, P.-A. Raviart, Finite element methods for Navier-Stokes equations, in: Theory and Algorithms, in: Springer Series in Computational Mathematics, vol. 5, Springer-Verlag, Berlin, 1986.
- [16] J. Könnö, D. Schötzau, R. Stenberg, Mixed finite element methods for problems with Robin boundary conditions, SIAM J. Numer. Anal. 49 (1) (2011) 285–308, https://doi.org/10.1137/09077970X.
- [17] D. Boffi, F. Brezzi, M. Fortin, Mixed Finite Element Methods and Applications, Springer Series in Computational Mathematics, vol. 44, Springer, Heidelberg, 2013.
- [18] S.C. Brenner, L.R. Scott, The Mathematical Theory of Finite Element Methods, 3rd edition, Texts in Applied Mathematics, vol. 15, Springer, New York, 2008.
- [19] D.A. Di Pietro, A. Ern, Mathematical Aspects of Discontinuous Galerkin Methods, Mathématiques & Applications (Berlin) [Mathematics & Applications], vol. 69, Springer, Heidelberg, 2012.
- [20] R.A. Adams, Sobolev Spaces, Pure and Applied Mathematics, vol. 65, Academic Press [Harcourt Brace Jovanovich, Publishers], New York-London, 1975.
- [21] L.C. Evans, Partial Differential Equations, Graduate Studies in Mathematics, vol. 19, American Mathematical Society, Providence, RI, 1998.
- [22] A.M. Stuart, Inverse problems: a Bayesian perspective, Acta Numer. 19 (2010) 451–559. https://doi.org/10.1017/S0962492910000061.
- [23] T. Bui-Thanh, O. Ghattas, J. Martin, G. Stadler, A computational framework for infinite-dimensional Bayesian inverse problems part I: the linearized case, with application to global seismic inversion, SIAM J. Sci. Comput. 35 (6) (2013) A2494–A2523, https://doi.org/10.1137/12089586X.
- [24] N. Halko, P.G. Martinsson, J.A. Tropp, Finding structure with randomness: probabilistic algorithms for constructing approximate matrix decompositions, SIAM Rev. 53 (2) (2011) 217–288, https://doi.org/10.1137/090771806.

- [25] A.K. Saibaba, J. Lee, P.K. Kitanidis, Randomized algorithms for generalized Hermitian eigenvalue problems with application to computing Karhunen-Loève expansion, Numer. Linear Algebra Appl. 23 (2) (2016) 314–339, https://doi.org/10.1002/nla.2026
- [26] N. Metropolis, A.W. Rosenbluth, M.N. Rosenbluth, A.H. Teller, E. Teller, Equation of state calculations by fast computing machines, J. Chem. Phys. 21 (6) (1953) 1087–1092, https://doi.org/10.1063/1.1699114.
- [27] W.K. Hastings, Monte Carlo sampling methods using Markov chains and their applications, Biometrika 57 (1) (1970) 97–109.
- [28] J. Martin, L.C. Wilcox, C. Burstedde, O. Ghattas, A stochastic Newton MCMC method for large-scale statistical inverse problems with application to seismic inversion, SIAM J. Sci. Comput. 34 (3) (2012) A1460–A1487, https://doi.org/10.1137/ 110845598
- [29] T. Bui-Thanh, M.A. Girolami, Solving large-scale PDE-constrained Bayesian inverse problems with Riemann manifold Hamiltonian Monte Carlo, Inverse Probl. Special Issue (2014) 114014.
- [30] T. Bui-Thanh, C. Burstedde, O. Ghattas, J. Martin, G. Stadler, L.C. Wilcox, Extreme-scale UQ for Bayesian inverse problems governed by PDEs, in: SC12: Proceedings of the International Conference for High Performance Computing, Networking, Storage and Analysis, 2012.
- [31] J. Nocedal, S.J. Wright, Numerical Optimization, 2nd edition, Springer Verlag, Berlin, Heidelberg, New York, 2006.